Report on the Performance Characterisation of Caesium Telluride Photocathodes P5 to P8 Manufactured at CERN and later Characterised at Daresbury Laboratory

L.B. Jones, H.M. Churn & T.C.Q. Noakes
Accelerator Science and Technology Centre
STFC Daresbury Laboratory
Warrington WA4 4AD, United Kingdom

L.A.J. Soomary
Department of Physics, University of Liverpool
Liverpool L69 7ZE, United Kingdom

C. Benjamin
Department of Physics, University of Warwick
Coventry CV4 7AL, United Kingdom

H. Panuganti, E. Chevallay, V. Fedosseev & M. Himmerlich
The European Organization for Nuclear Research (CERN)
1211 Geneva 23, Switzerland

Summary

In this report we present data on 4 caesium telluride cathodes synthesized at CERN and characterised at STFC Daresbury Laboratory. The characterisation involved measuring the surface composition of each cathode using X–ray Photoelectron Spectroscopy (XPS), surface roughness measurements with an in–vacuum Scanning Tunnelling Microscope (STM) and Quantum Efficiency (QE) measurements on the Multiprobe system. Performance analysis was carried out on the Transverse Energy Spread Spectrometer (TESS) at room and cryogenic temperatures, extracting the Mean Transverse Energy (MTE) of each cathode from their Transverse Energy Distribution Curves (TEDC).

Contents

0   Project Overview

The aim of this collaborative project between the photocathode teams based at the STFC Daresbury Laboratory and at CERN was to prepare Cs–Te photocathodes at CERN using the CLIC preparation facility following procedures developed over many years, then transport these under vacuum to Daresbury in order to carry out a rigourous set of performance characterisation measurements to establish the energy spread of the photoemitted electrons and the physical and chemical nature of the photoemissive surface.

Photocathodes were prepared and characterised by the Daresbury team to verify sample cleanliness through X–ray Photoemission Spectroscopy (XPS) and surface roughness using Scanning Tunnelling Microscopy (STM), then transported to CERN in a vacuum suitcase for deposition of the photoemissive layer. Quantum Efficiency (QE) measurements at CERN immediately after photocathode growth were not possible as the cathode holders used by the Daresbury equipment are not compatible with the QE measurement chamber at CERN, so any initial QE estimate and photocathode 'quality' was inferred through experience of the deposition process.

The finished photocathodes were loaded directly into an XHV vacuum suitcase and transported overland to Daresbury where they were subjected to photoemission performance testing in the Transverse Energy Spread Spectrometer (TESS) and a second round of surface characterisation measurements (where possible) using XPS, STM and QE.

1   Photocathode Preparation

Four polycrystalline copper substrate 'pucks' were supplied by SPL, polished to a surface roughness of $R_a < 30$ nm. The pucks were mounted into photocathode holders before being characterised in the Multiprobe experimental system [1] with the following measurements carried out:

- X–ray Photoelectron Spectroscopy (XPS) to determine the surface chemistry;

- Scanning Tunnelling Microscope (STM) to determine the surface roughness (R_a);

- Quantum Efficiency (QE) under illumination at 265 nm.

The results of pre–deposition QE tests on the bare copper pucks was very low as the workfunction of this surface is more than the 4.64 eV photon energy delivered by the UV LED. The large energy spread in the LED output and the non–step nature of the Fermi edge resulted in a low but measurable photocurrent arising from the higher–energy photons delivered by the LED, but this returned an artificially–reduced value for QE as the optical power measurement used in the QE calculation included all of the photon output. Consequently, the initial QE levels measured from the bare copper substrates was typically 4×10^{-6} at 265 nm.

1.1 X–ray Photoelectron Spectroscopy (XPS)

XPS spectra were obtained with the sample illuminated using a PSP Vacuum Technology TX400 X–ray source delivering unmonochromated Mg K_α radiation with $\varepsilon = 1,253.6\,\text{eV}$. Photoemission spectra were measured using the VG Alpha 110 hemispheric electron energy analyser. Survey and core region spectra were acquired using a pass energy of 50 eV and 20 eV respectively. Calibration of the analyser was carried out using a polycrystalline Ag sample to experimentally determine the analyser transmission function, following the method outline by Ruffieux *et al.* [2], and the analyser work function was determined using a fit of the Ag sample Fermi edge.

Analysis was carried out using the CasaXPS[1] software package using a mix of Gaussian–Lorentzian functions and a standard Shirley background across all cathodes for all spectra discussed, following best–practice for the analysis of XPS data [3]. All reference binding energies used for curve fitting were taken from the NIST X–ray Photoelectron Database [4]. Relative Sensitivity Factors (RSFs) derived from the Scofield cross–sections [5] were used to scale the peak areas such that the intensity is relative to the C 1s. This facilitated meaningful peak fitting and elemental composition analysis.

1.2 Scanning Tunnelling Microscopy (STM)

An Omicron AFM/STM was used to measure the mean surface roughness (R_a) of the photocathode substrate to verify that this was as expected prior to deposition of the photoemissive layer. Data was taken at the substrate centre and at various radial displacements to establish confidence in the measurement.

1.3 Quantum Efficiency (QE)

Quantum efficiency (QE) was measured in the Multiprobe chamber, with the photocathode illuminated at a wavelength of either 265 nm by a UV LED[1], or at 266 nm by a UV laser[2]. The light from both of these sources entered the vacuum chamber through a viewport with a measured transmission level of 10 % at 266 nm.

The LED source delivers a nominal 0.5 mW of UV power at a wavelength of 265 nm with a spectral range of 11 nm FWHM into an emission cone with a 4° half–angle. The beam was collected and focused onto the photocathode sample with a single Thorlabs LB4265–UV (25 mm diameter, $f = 150$ mm) biconcave UVFS AR–coated lens with an effective focal length of 138.1 mm at 265 nm. The power was measured in air using a ThorLabs PM400 power meter and a S401C (1 μW resolution) thermal power sensor. The sensor was placed close to the beam focal point at a position with equivalent distance to the photocathode when located inside the vacuum chamber. It was found to be 0.1 mW. A correction to account for the 10 % transmission through the vacuum viewport was applied, so the estimated optical power falling onto the photocathode was 10 μW.

The UV laser generates a 1 kHz train of 1 ns pulses at a wavelength of 266 nm, delivering an average power of 12 mW. The beam is heavily attenuated to avoid space–charge

---

[1]Roithner LaserTeknik GmBH DUV–HL5NR @ 265 nm.
[2]Crylas GmBH FQSS 266–Q4

4

conditions during photoemission which would result in an incorrect photocurrent measurement, and thus affect the QE. To attenuate the beam, it is passed through a $\times 3$ beam expander, and then through a 1 mm diameter aperture placed at the centre of the expanded beam. To further attenuate the optical power to the level where no space charge effects are found, the beam is passed though an OD 2.0 reflective filter.

During QE measurement, a charge extractor electrode mounted on a Z–stage is moved into close proximity with the photocathode, approximately 10 mm from the surface. The DC bias on the charge collector was progressively increased until we saw saturation in the measured photocurrent, thus demonstrating that the photocurrent measurement was made on the full extracted charge from the photocathode sample. This bias to achieve this was typically at the $+500$ V level.

Photocurrent was measured as the total yield from the photocathode sample. During the measurement, the sample may be at earth potential, or at some negative bias of -9 V or -18 V by measuring through a battery bias box. When using the unmodulated CW output of the UV LED, the photocurrent was measured using a Keithley model 6485 picoammeter. When using the UV laser, a timing signal was taken from the laser such that phase–sensitive detection was employed using a Stanford Research SR–830 lock-in amplifier.

$$QE_\lambda = \frac{n_e}{n_p} = \frac{124 \times I_p}{\lambda \times P_{opt}} \tag{1}$$

QE was calculated using equation (1) where n_e and n_p are the number of emitted electrons and incident photons respectively, I_p is the photocurrent in nA, λ is the illumination wavelength in nm and P_{opt} the optical power falling on the photocathode surface in μW.

1.4   Vacuum Suitcase

The substrate pucks and finished photocathodes were transported between the Daresbury and CERN Laboratories in an XHV vacuum suitcase, as shown in Fig. 1. The suitcase design is centred on a small 4–way cross vessel with a gate valve[3] providing vacuum isolation. The suitcase houses a magazine with the capacity to hold up to 4 photocathodes mounted on 19 mm Omicron sample plates, as shown in detail in Fig. 1 (right). The magazine is mounted on a magnetic linear transfer arm. The suitcase incorporates a combined ion/NEG pump[4] as can be seen in Fig. 1 (left). The final port can be closed with a viewport to aid sample handling, but in this work it was removed and replaced with an additional NEG pump[5] to increase pumping speed during suitcase transportation.

During transit, ion pump operation was maintained using a battery–powered high voltage power supply specifically designed for this purpose[6]. An additional large–capacity battery was included in the transit crate to ensure a consistent electrical supply throughout the journey. The LSA 2.1 provides the necessary voltage to optimally drive the ion

---

[3]VAT 48.2 series DN63CF-F hand–operated all–metal gate valve (model # 48236–CE05).
[4]SAES Getters NEXTorr D 100-5.
[5]SAES Getters CAPACITORR D 50.
[6]FerroVac GmBH LSA 2.1 battery operated high voltage controller for ion gettering pumps.
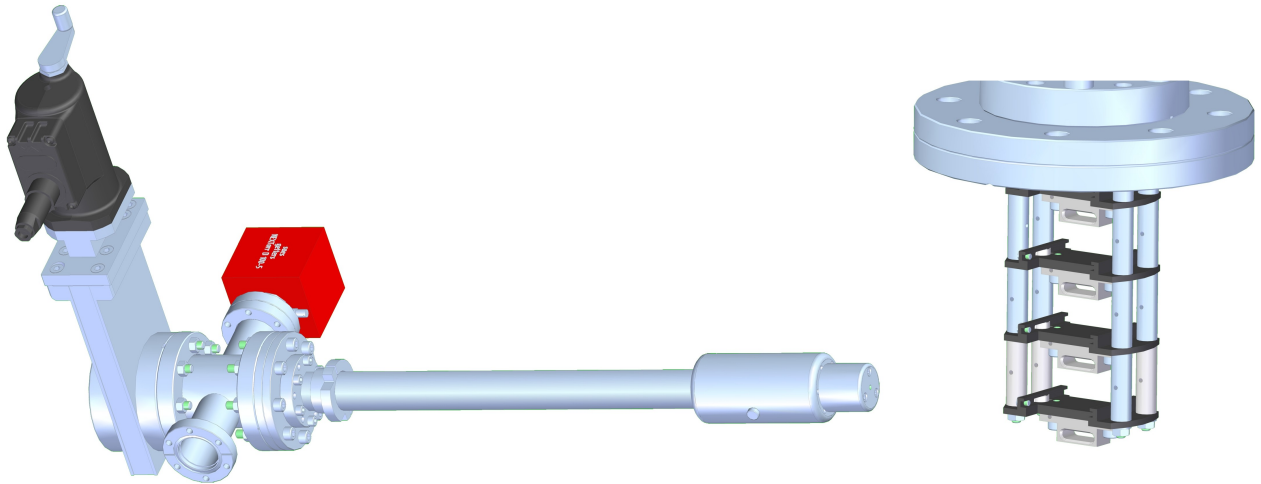
Figure 1: **(Left)** Schematic detail of the XHV vacuum suitcase used for photocathode transportation. **(Right)** Magazine in detail showing capacity for up to 4 photocathodes.

pump. It also measures the current drawn by the pump and converts this to pressure, and so provides a means of monitoring the vacuum within the suitcase.

The LSA 2.1 unit was modified to provide an analogue output of the pump current, and thus facilitate monitoring to record the vacuum history during suitcase transit. A data logger[7] which recorded the pump current analogue up to three times per second was included in the transit crate. Data logging was initiated when the transit crate was closed at CERN, and subsequently stopped when the crate was opened at Daresbury. The data was downloaded and the vacuum history plotted for the entire journey, with the integral extracted from this data to estimate the total gas exposure in Langmuirs (L).

The NEG pumps were conditioned at CERN following the final bake of the system prior to the commencement of photocathode deposition, thus maximising the gas capacity of these devices. The ion pump was also conditioned at this time.

During conditioning with the ion pump at its full 5.00 kV operating voltage, a series of pressure spikes were observed. This implied the presence of a small field emitter on one of the ion pump HV electrodes which was arcing periodically. To avoid further discharges, the operating voltage was reduced to 4.05 kV, thus suppressing the HV discharges and associated pressure spikes. This flexibility of operation was only possible using the SAES power supply.

However, it was not possible to reduce the output voltage of the battery–powered LSA 2.1 supply which would be used to maintain vacuum during transportation, so the ion pump operating voltage was reset to 5.00 kV. It was noted that over time, the discharges and associated vacuum events decreased in frequency, and eventually stopped so it is assumed that this extended period of operation while the photocathodes were prepared was sufficient to condition the electrodes and remove the field emitter.

---

[7]Chauvin Arnoux L452 2–channel data logger.

2 Photocathode Deposition

The CLIC photocathode preparation facility was used to deposit photoemissive caesium telluride (Cs–Te) films onto the copper pucks, following established procedures [6, 7]. The deposition order was noted by the CERN team, and the designations P5 to P8 reflect the order in which the photocathodes were manufactured. The depositions were carried out at room temperature, and details of the elemental thicknesses logged are shown in Table 1 with the complete deposition histories shown in Fig. 2.

Cathode	Cs Thickness [nm]	Te Thickness [nm]	Substrate Temperature [°C]
P5	37.6	12.8	21.0
P6	86.6	33.7	21.0
P7	57.2	20.2	23.5
P8	38.2	25.9	21.5

Table 1: Total film thicknesses of Cs and Te deposited on each photocathode surface.

It was not possible to measure QE at CERN immediately after photocathode growth as the Omicron–style cathode holders used by the experimental systems at Daresbury are not compatible with the QE measurement chamber at CERN. Based on their experience of previous deposition processes and photocathode 'quality', the CERN team estimate that the initial QE of the P5 photocathode was in the region of 10 %.
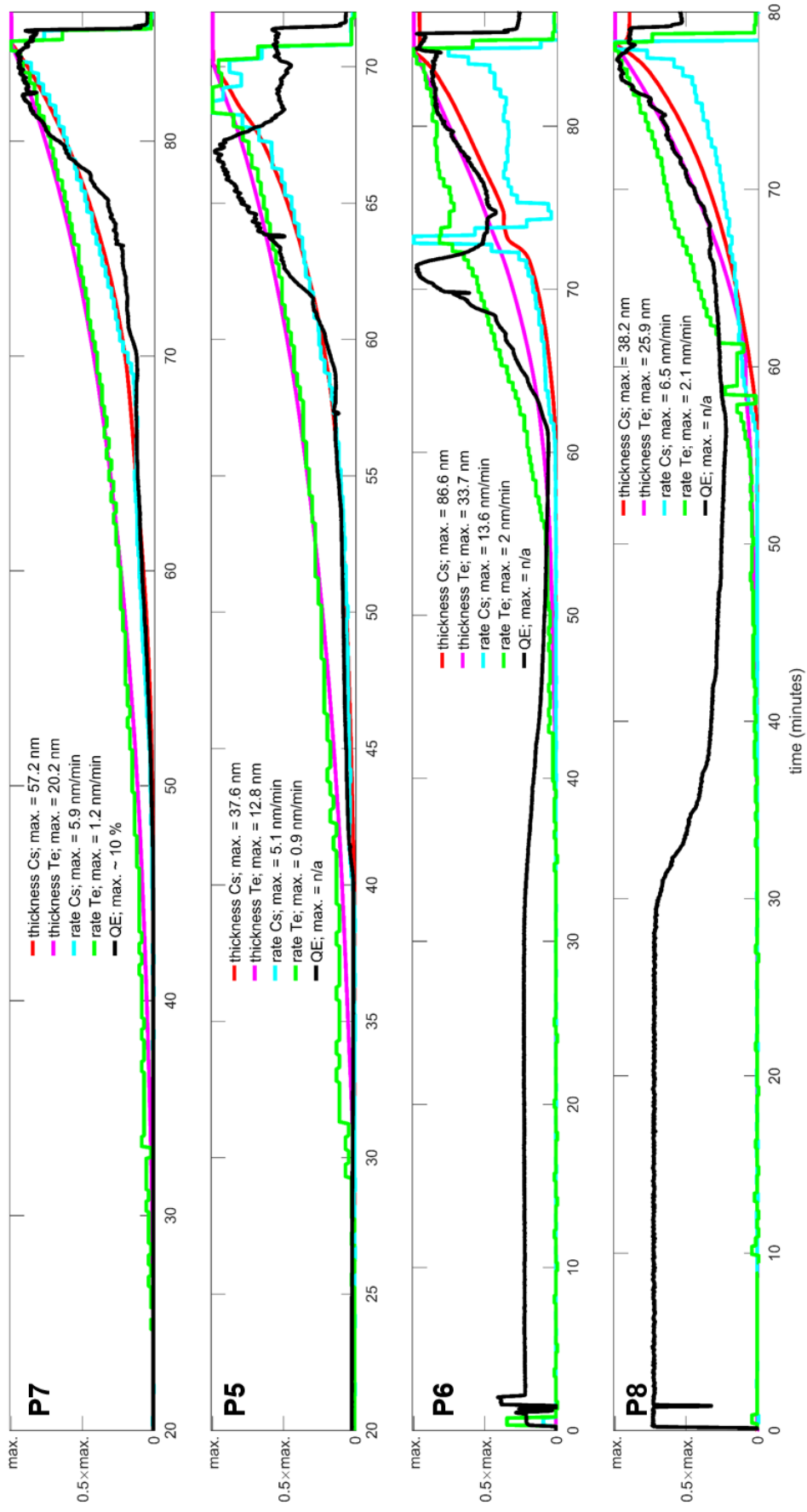
Figure 2: Deposition process summary showing elemental deposition rates and total thickness data for each photocathode.

3 Photocathode Transportation and Receipt

The finished photocathodes were loaded into the vacuum suitcase described in section 1.4. this was connected directly to the preparation chamber. The final photocathode was loaded Friday 18 June, 2021, and the suitcase disconnected from the preparation facility. The suitcase was re–packed into its transit case, with the ion pump connected to its battery–operated power supply and the data logging function initiated. The crate containing the suitcase was moved from the CLIC photocathode laboratory to the CERN logistics depot at Prévessin that afternoon, and the consignment remained there over the weekend.

The consignment was collected from CERN on Monday 21 June, and transported overland from CERN directly to Daresbury Laboratory with the journey completed in less than 24 hours. On receipt at Daresbury, the crate was moved immediately to the VISTA laboratory area and opened so that the contents could be inspected. No issues were identified. The pressure data logging was stopped and the suitcase was then removed from the crate and mounted onto the III–V photocathode preparation facility (PPF) loading chamber [11]. At this point, the LSA 2.1 battery power supply to the ion pump was replaced with the conventional mains–powered SAES version.

The pressure data log was examined and the history plotted to establish the vacuum conditions between the vacuum suitcase being packed in its crate at CERN, and the crate being received at Daresbury. This is shown in Fig. 3. The data shows that while there had been some pressure excursions, the average pressure throughout the time that the suitcase was maintained by the battery power supply was in the region of 8×10^{-11} mbar and the total gas exposure estimated from the integral of the vacuum log is 28 Langmuirs. It should be noted that the vacuum system was well–baked, so the majority of the gas to
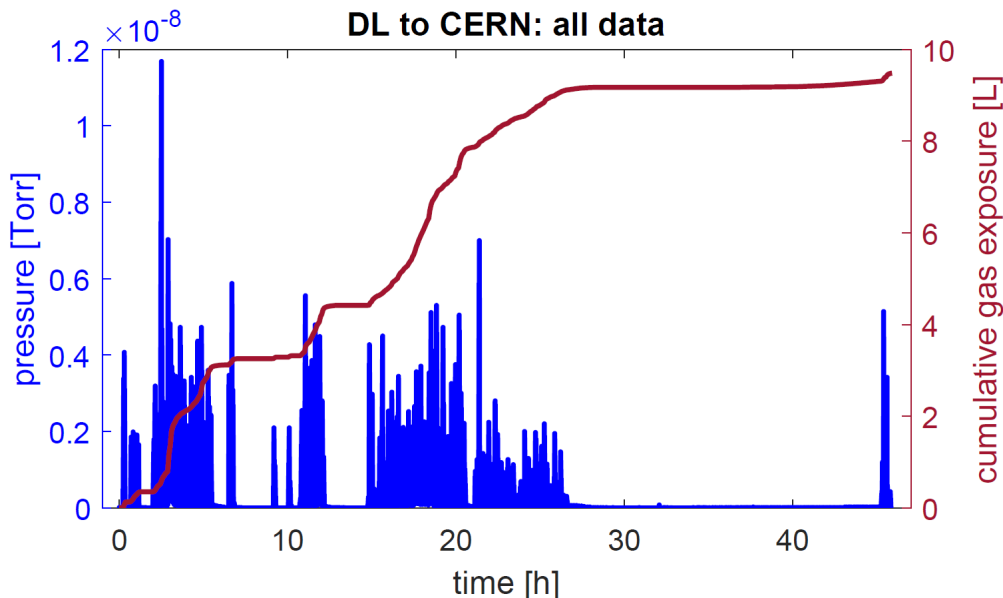

Figure 3: Vacuum suitcase pressure log between loading the suitcase into its transit crate at CERN on Friday 18 June and subsequent unloading at Daresbury on Tuesday 22 June.

which the photocathodes were exposed would be hydrogen with a lesser amount of nitrogen, oxygen and oxygen–containing species such as carbon dioxide, carbon monoxide and water. The vacuum recovery following pressure spikes was rapid, and the magnitude of the spikes themselves moderate, so we assume that contamination was

The photocathodes were sequentially unloaded into the III–V PPF and stored under XHV conditions, typically around 5×10^{-12} mbar. During transfer, the photocathodes were photographed under ostensibly the same lighting and exposure conditions. Fig. 4 shows the photocathodes as–received at Daresbury Laboratory. The colour differences imply variance in the thickness and composition of the deposited photoemissive layer, and it is expected that this will lead to differences in their performance characteristics.
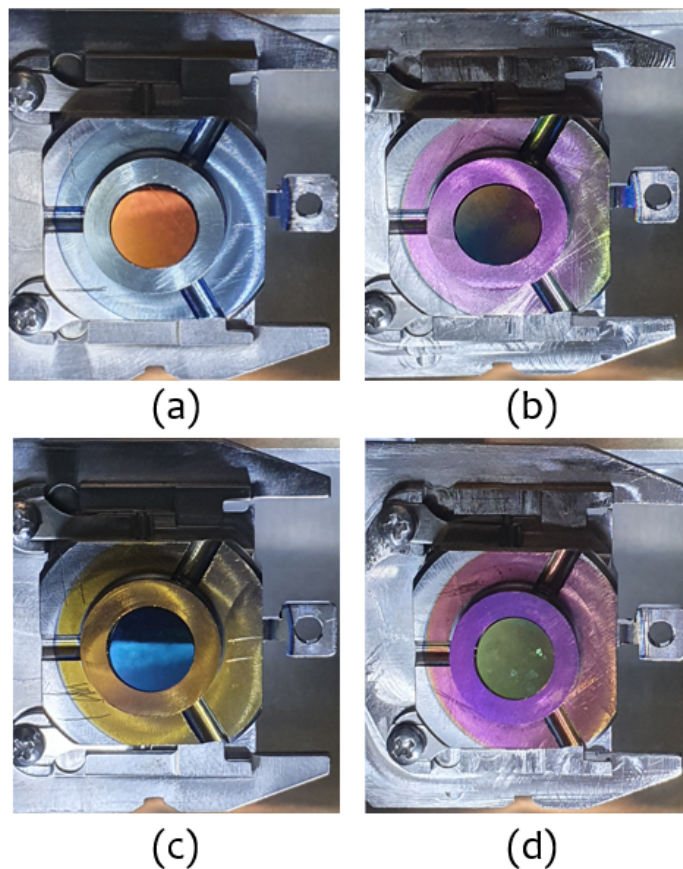

Figure 4: Photographs acquired under the same lighting and camera conditions of the 4 Cs–Te cathodes during transfer from the vacuum suitcase into the III–V PPF where:
(a) is the P5 photocathode (CERN # 225);
(b) is the P6 photocathode (CERN # 226);
(c) is the P7 photocathode (CERN # 224);
(d) is the P8 photocathode (CERN # 227).
The colour differences at visible wavelengths are due to differences in the thickness of the photoemissive layer and the elemental composition of the surface.

4 Photocathode Performance Characterisation

Each photocathode was subjected to a series of MTE measurements in the TESS system [12] at both room and cryogenic temperatures. Once MTE measurements were complete, the photocathodes were then transferred to the Multiprobe system [1] using the vacuum suitcase to carry out a second set of surface characterisation measurements, as described in section 1.

The MTE measurement was carried out first as the vacuum in the PPF and the TESS systems is superior to that of the Multiprobe by 2 or more orders of magnitude, so the rate of photocathode degradation will be commensurately reduced under such storage conditions.

This suite of measurements was carried out for all photocathode samples, except for P5 which was unavoidably exposed to atmosphere after it was dropped inside the TESS necessitating a venting of the vacuum system for its manual retrieval.

The order in which the photocathodes were characterised was P5, then P7, then P8 and finally P6. A problem with the STM which occurred during surface roughness measurements on the P8 photocathode prevented any further STM measurements, so we have no surface roughness data for the P6 Cs-Te photocathode.

This report summarises the work done in characterising the cathodes shown in Fig. 4, and considers reasons for the notable differences found in MTE and spectral response. We link these differences to the clear variability in the surface colour, the deposition thickness data shown in Table 1, and the interpretation of the post–deposition XPS measurements.

4.1 Relative Quantum Efficiency

Photoemission image data obtained from the TESS was also used to estimate the QE for each photocathode and permit relative comparisons over a range of illumination wavelengths. This was accomplished by combining the illumination intensity (optical power) with the detector chain settings to assess the overall gain in the TESS measurement, and then using this to normalise the integrated photoemission footprint. In a characterisation measurement, the gain provided by the TESS detector MCP was measured found to double for each $41.0 \pm 0.4\,\text{V}$ increase in the potential difference between the MCP front and MCP back over the linear region of the MCP response curve. Therefore the MCP gain (G_{mcp}) over this linear region can be estimated by:

$$G_{mcp} = 2^{\left(\frac{\Delta V_{mcp}}{41.0}\right)} \tag{2}$$

where ΔV_{mcp} is the voltage difference between the MCP back and front plates given by $(V_{mcpB} - V_{mcpF})$. The relative QE ($QE_{relative}$) is then calculated using Equation (3):

$$QE_{relative} = \frac{I_{corrected}}{t \cdot (P_{opt} \times T_{viewport}) \cdot G_{mcp}} \tag{3}$$

where $I_{corrected}$ is the total photoemission image intensity after the dark image has been subtracted from the data image, t is the data acquisition exposure time, P_{opt} is the optical power measured immediately before the sapphire viewport into the TESS vacuum

chamber, and $T_{viewport}$ is the wavelength–dependent transmission through the uncoated sapphire viewport.

This approach does not yield an absolute value for QE at any specific wavelength. It serves as a useful mechanism for making meaningful comparisons of the photoemissive output of different cathodes at different wavelengths.

4.2 Order of Photocathode Analysis

The photocathodes were analysed in the order P5 $\rightarrow$ P7 $\rightarrow$ P8 $\rightarrow$ P6. There are two fundamental issues which impacted our aspirations to carry out all of the documented characterisation work on each of the cathodes:

1. The P5 cathode was tested first, but at the end of work to characterise its photoemission properties, it was dropped inside the TESS chamber. Its recovery necessitated venting of the TESS system, so it was not possible to acquire any meaningful data relating to the chemical analysis of its surface. STM surface roughness measurements were carried out, as were SEM measurements, but meaningful absolute QE measurement was not possible.

2. The STM tip broke after the first surface roughness measurement at the centre of the P7 photocathode. During replacement of the STM tip, the STM tip holder broke thus rendering the STM system unserviceable. This prevented any further surface roughness measurements on the P7 cathode, and prevented us from making any STM measurements on the P6 cathode.

5 P5 CsTe Cathode

While P5 was the first photocathode to be characterised and received a full and detailed MTE analysis (shown in section 5.3), the sample was dropped inside the TESS and was subsequently exposed to the atmosphere during its recovery. The XPS and STM data are therefore not reflective of the original chemical composition and surface state, but this work was carried out anyway for the purposes of completeness. However, we believe that the surface roughness has not been adversely affected by this atmospheric exposure, so while the XPS data has limited value, the surface roughness measurements remain valid.

5.1 XPS Surface Analysis

Fig. 5 shows the survey scan of P5. Notable elemental peaks are labelled with all other features corresponding to further core regions, Auger and electron loss features. Cs, Te, C, O and Cu are all present in the spectra, and the significant amounts of O and C present are clearly linked to its atmospheric exposure.

Core regions scans were acquired for quantification and to determine chemical composition. Table 2 shows the elemental composition of the Cs–Te film utilising the Cs and Te 3d core regions.

Using data for the 3d states over a sampling depth of around 3.9 nm, we estimate that the Cs:Te ratio in this heavily oxidised photocathode is 3:1 . This sampling depth is defined as the depth from which 95% of all photoelectrons are scattered by the time they reach the surface of the sample, and is typically $3\lambda_{mfp}$ where λ_{mfp} is the mean free path of an electron in a solid. This suggests that the film has excess caesium in the surface region is likely to be a contributing factor to the photoemission seen at longer illumination wavelengths which is discussed later in the MTE analysis.

Region	Peak Position [eV]	RSF	At Conc. [%]
Cs 3d	724.70	38.73	14.06
Te 3d	573.15	29.91	4.65
C 1s	285.25	1.00	31.08
O 1s	530.90	2.85	50.21

Table 2: Surface elemental composition for the P5 photocathode determined using XPS from the core region components. The sampling depth is estimated to be 3.9 nm for the 3d regions.
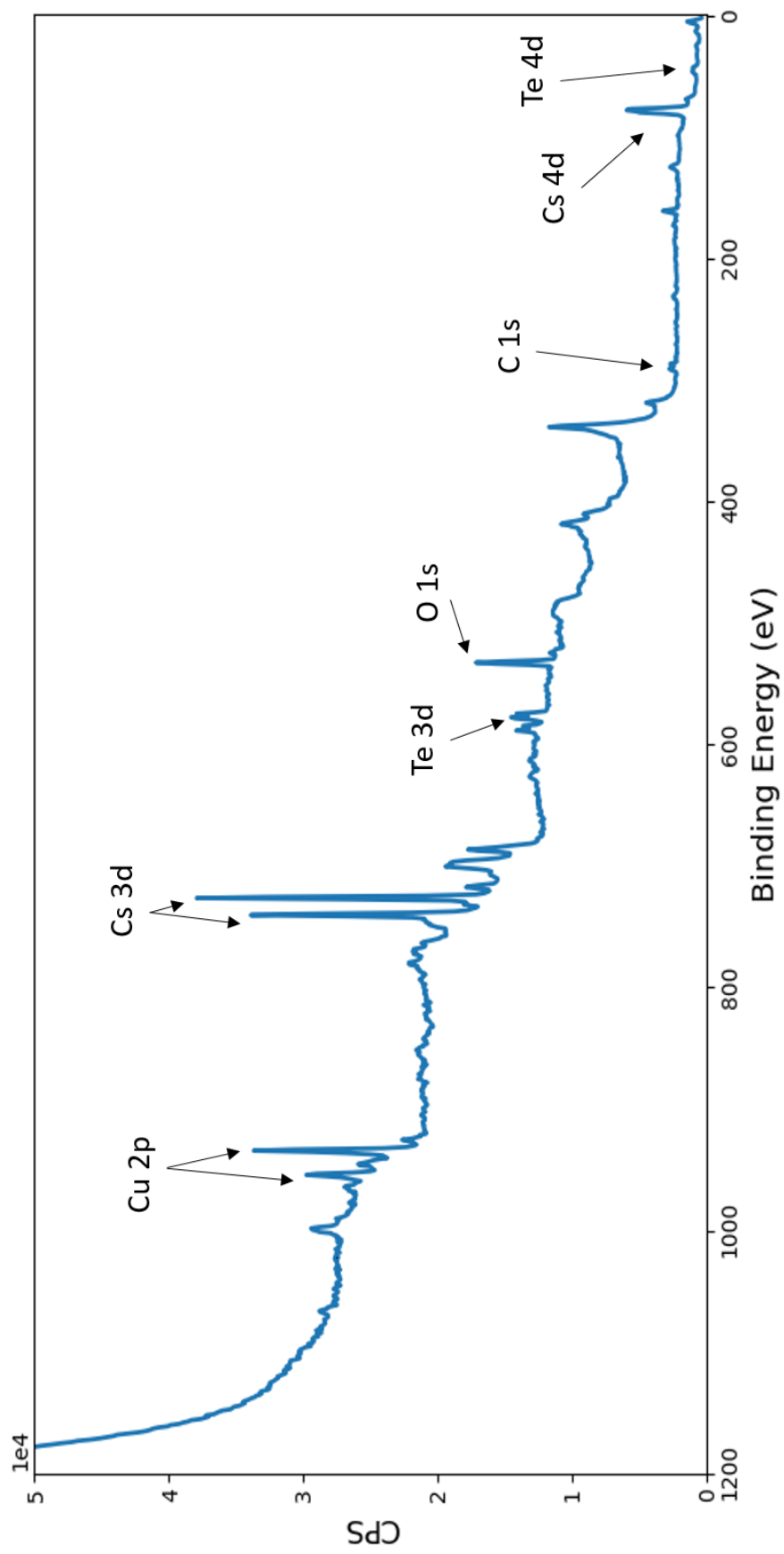
Figure 5: XPS survey spectrum for the P5 photocathode. The source used was a Mg K$_\alpha$ (1,253.6 eV) with 50 eV pass energy.

5.2   Surface Topography

The P5 surface topography was analysed using two techniques; SEM and STM. We utilised Scanning Electron Microscopy (SEM) as a final ex–vacuum measurement on the P5 photocathode to investigate overall sample texture on a micron scale. Fig. 6a shows a $60 \times 60\,\mu$m scale SEM image near the centre of the P5 photocathode which exhibits significant texture on the micron scale. Resolving the surface further as shown in Fig. 6b, the grain sizes of the Cs–Te film are observed to be smaller than a micron inferring a low surface roughness.
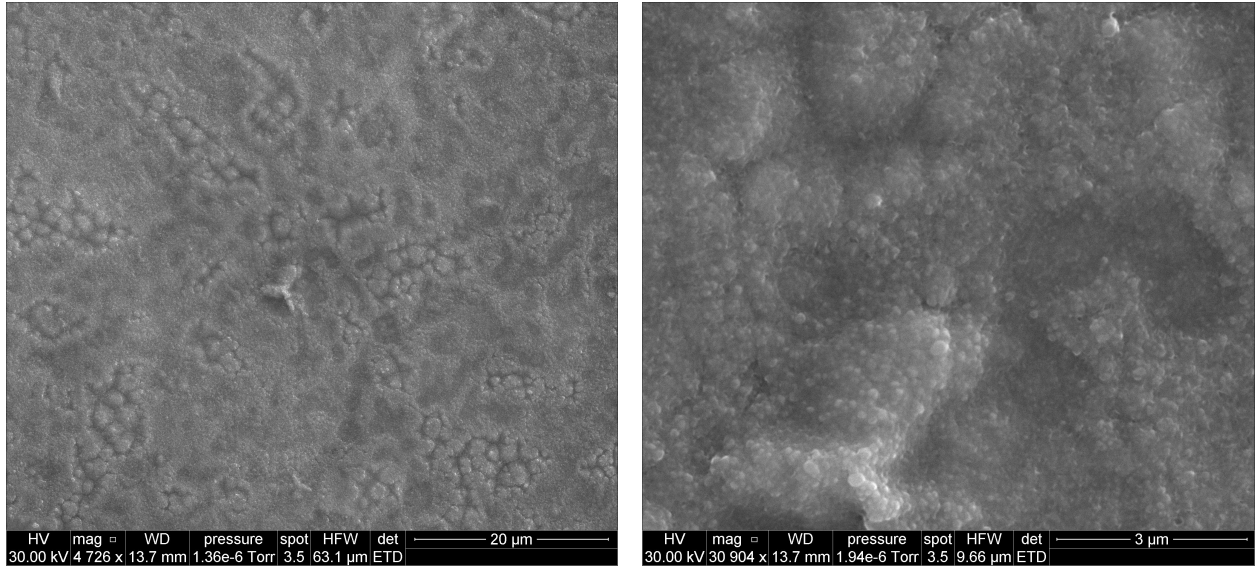
(a) Large area $60 \times 60\,\mu$m SEM image at the centre of the P5 photocathode surface.

(b) High magnification SEM image at the centre of the P5 photocathode showing Cs–Te grains.

Figure 6: SEM images of the P5 photocathode centre at different magnification scales.

Three positions were investigated using STM, with position 1 being the centre of the P5 photocathode and position 3 the largest possible radial displacement of the STM tip from the centre of P5. Table 3 summarises the RMS and mean surface roughness for each position calculated using Gwyddion [13]. The STM images shown in Fig. 7 were taken at positions 1, 2 and 3 respectively. The surface roughness is lowest at the cathode

Position	RMS Roughness, R_q [nm]	Mean Roughness, R_a [nm]
1	6.1	4.5
2	12.3	10.5
3	11.1	9.0

Table 3: Summary of surface roughness measurements for the P5 photocathode. Position '1' relates to the geometric centre of the photocathode, with '2' and '3' relating to positions with increasing radial displacement from the centre. All measurements were made by STM over a $500 \times 500\,\text{nm}^2$ area.

centre with a measured RMS of 6.1 nm. There is a sharp increase in roughness to around 12.0 nm as we move outwards to positions two and three. Fig. 7c shows that the grain size increases progressively with radial displacement from the P5 centre, rising from less than 100 nm to around 200 nm.
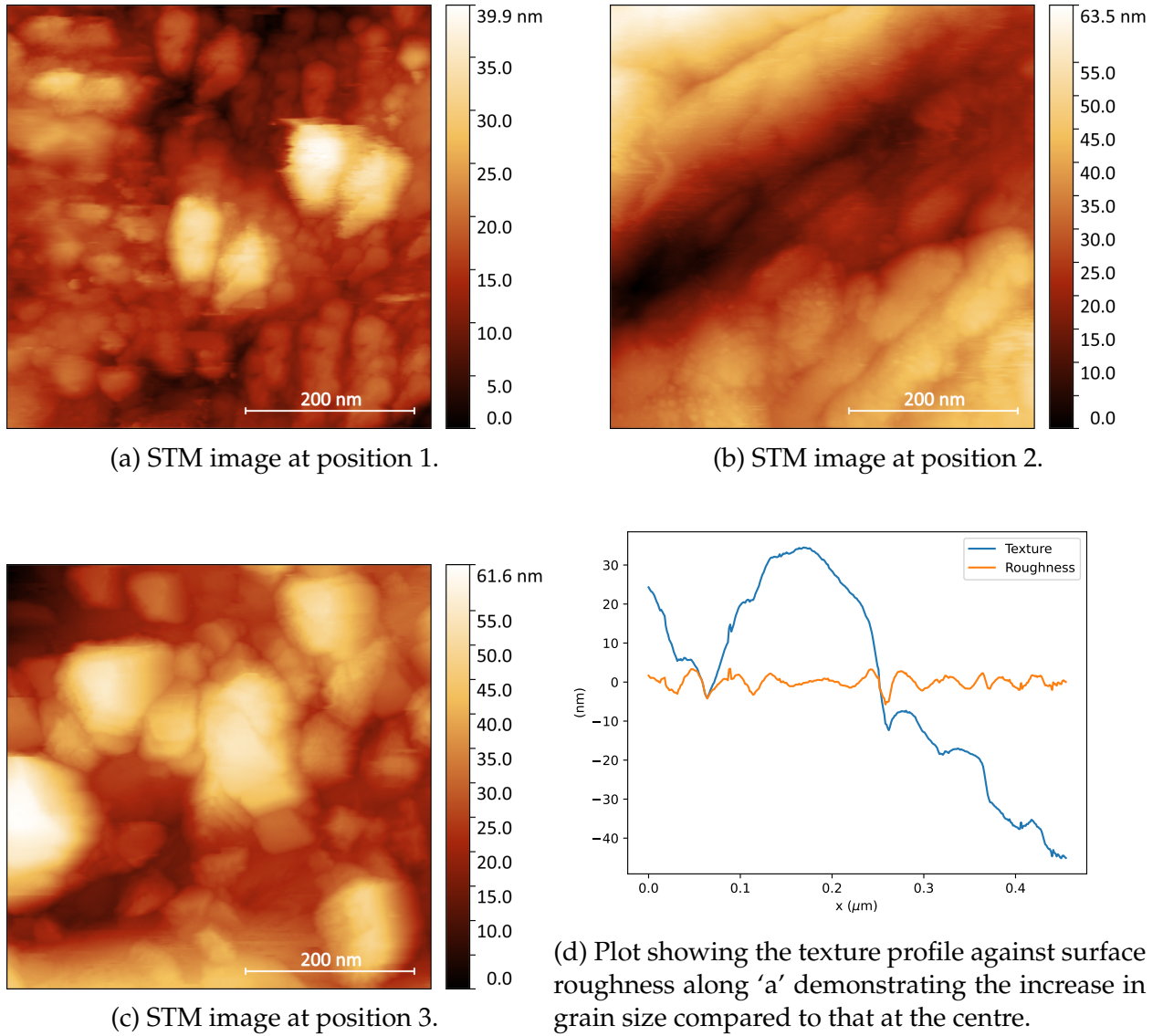

(a) STM image at position 1.

(b) STM image at position 2.

(c) STM image at position 3.

(d) Plot showing the texture profile against surface roughness along 'a' demonstrating the increase in grain size compared to that at the centre.

Figure 7: 500 nm × 500 nm STM image data for the P5 photocathode at 3 positions.

5.3 MTE Analysis

Fig. 8 shows the MTE values measured as a function of the illumination wavelength for the P5 Cs–Te cathode at room temperature (red diamonds) and under cryogenic cooling at 178 K (blue diamonds). An OD 0.6 filter was installed after the monochromator for measurements over the wavelength range 236 – 326 nm. An OD 0.2 filter was used over the range 336 – 611 nm. Measurements at wavelengths beyond 400 nm also included a

16

long–pass filter to ensure suppression of any UV leakage or second–order light from the monochromator.

At room temperature the P5 cathode shows a progressive decrease in MTE under illumination at UV wavelengths before reaching a minimum MTE value of 57 ± 6 meV at 356 nm. This minimum is close to the measured spectral response for high–quality Cs_2Te photocathodes grown at BNL which exhibit an emission threshold around $340 - 350$ nm [9, 10]. However, photoemission was clearly seen at 386 nm with the MTE measured as 370 ± 35 meV. The MTE was seen to progressively decrease thereafter before ultimately reaching a minimum of 31 ± 3 meV at 611 nm. No photoemission was detected at longer wavelengths, though we note that the minimum MTE measured is close to the 25 meV thermal floor defined by $k_B T$ at room temperature.

Measurements taken under cryogenic conditions at 178 K over the wavelength range $236 - 326$ nm followed a broadly similar trend to those obtained at room temperature. The measured data points generally exhibit a lower MTE than room temperature measurements at the same illumination wavelength, with a minimum MTE of 70 ± 7 meV achieved at 316 nm. Further data with the P5 photocathode cryogenically cooled could not be acquired due to the photocathode being dropped inside the TESS vacuum chamber.

Fig. 9 reproduces the MTE data with the estimated relative QE overlaid, as estimated using Equation (3). Based on the chemical stoichiometry shown in Table 2, and recognising the fact that this data was obtained following oxidation of the P5 to atmosphere for recovery from the TESS vacuum chamber, we believe that photoemission from elemental caesium was responsible for the clear but unexpected emission at longer illumination wavelengths. The high measured MTEs result from caesium's extremely low workfunction, though it can be seen that the relative contribution of this element to the overall emission spectra is small, being several orders of magnitude lower than that from the dominant Cs–Te emitting species.
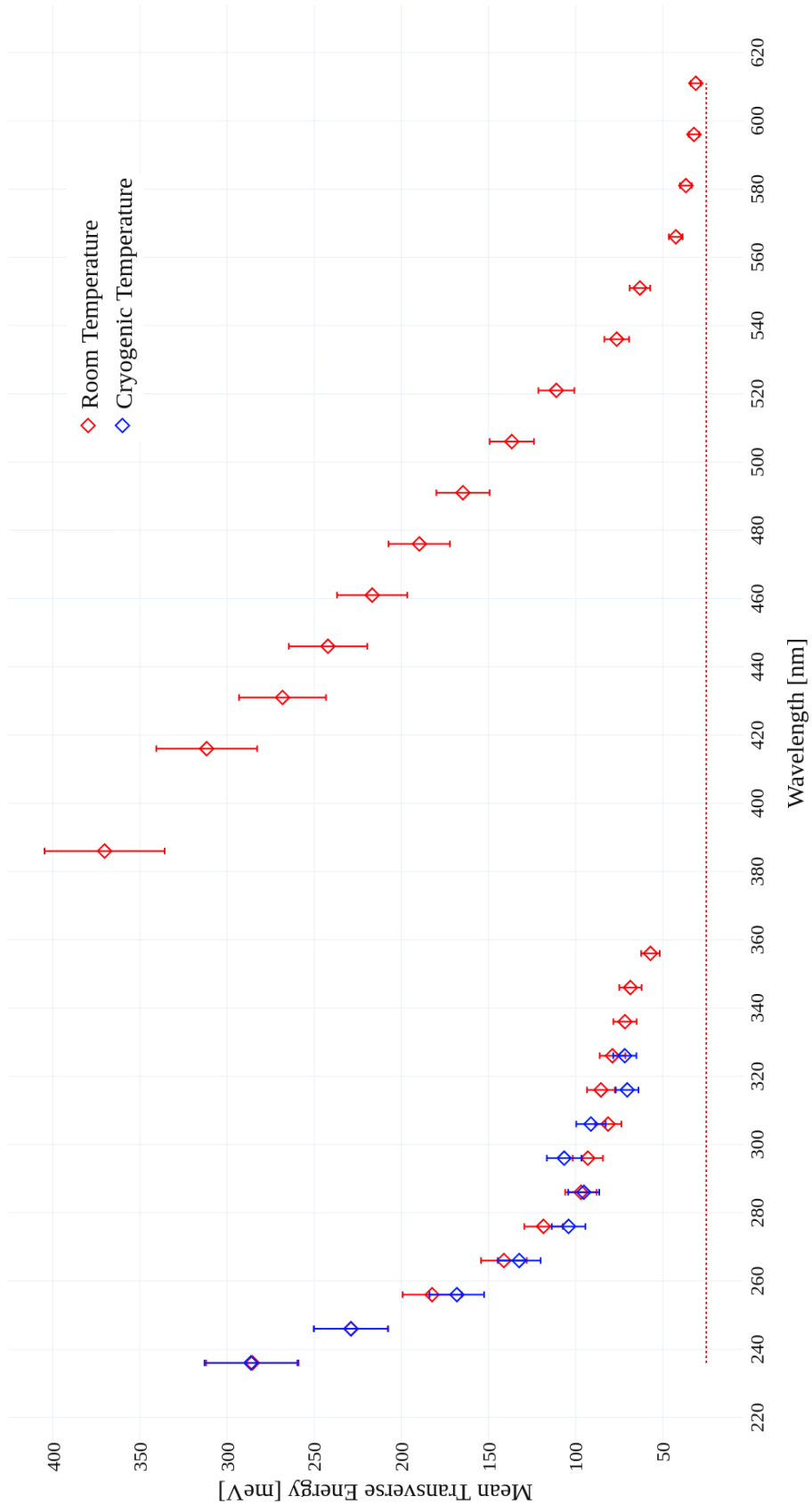
Figure 8: MTE measurements for the P5 Cs–Te photocathode under illumination at wavelengths between 236 nm and 611 nm for room temperature, and up to 336 nm under cryogenic conditions.
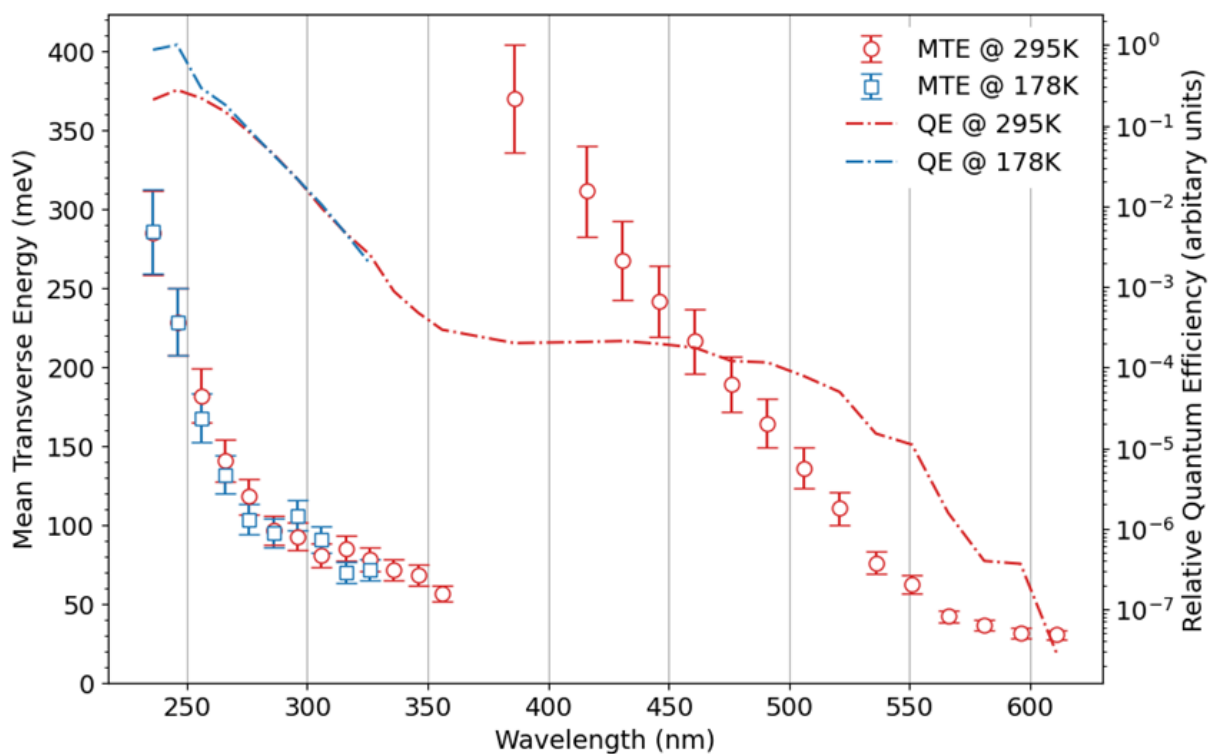
Figure 9: Measured P5 MTE values (left scale) with relative QE (right scale) overlaid to demonstrate the relative contribution (see section 4.1) of the photoemissive elements as the illumination wavelength is increased.

6 P6 CsTe Cathode

6.1 XPS Surface Analysis

Table 4 shows the overall elemental composition for the P6 photocathode surface, and Table 5 shows the specific bonding environments of those elements present. Fig. 10 shows the core elemental regions of P6 with peak fitting. The XPS spectra acquired for the P6 cathode showed oxygen and carbon contamination with an atomic concentration of 6.20 % and 4.18 % respectively.

A survey scan showed that the only elements present on the cathode surface were Cs, Te, O and C. While O and C each contribute a small percentage to the overall composition of the P6 photocathode, it must be noted that they ultimately reduce the Cs contribution to Cs_xTe ratio. The line shape of the O 1s shown in Fig. 10d suggests that the oxygen is in two different bonding environments: an organic carbon and CsO. This is also evidenced by the broadening of the Cs 3d profile in Fig. 10a, and also when cross–referenced to the P8 photocathode where the oxygen was not present.

| Region	At Conc. [%]
Cs 3d	54.26
Te 3d	35.34
O 1s	6.20
C 1s	4.18

Table 4: XPS overall elemental composition for the P6 photocathode calculated from the core region components.

| Region	Bonding Environment	Peak Position [eV]	FWHM	At Conc. [%]
Cs 3d$^{5/2}$	Cs_xTe	725.87	1.68	49.16
3d$^{3/2}$		739.84	1.68	
3d$^{5/2}$	Cs_2O	726.77	1.76	5.12
3d$^{3/2}$		740.54	1.76	
Te 3d$^{5/2}$	Cs_xTe	572.32	1.67	35.34
3d$^{3/2}$		582.67	1.67	
O 1s	Cs_2O	531.21	1.60	2.07
	C=O	532.33	1.99	4.13
C 1s	C=O	286.93	1.42	4.18

Table 5: XPS elemental composition for the P6 photocathode with bonding environments assigned according to the data–fitting shown in Fig. 10.
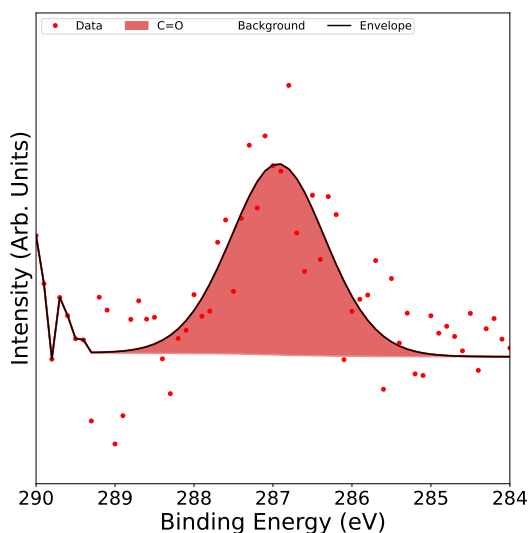
6.2   Bonding Environment Analysis

The Te 3d spectra has only one distinguishable peak at 572.32 eV. This is assumed to be in $Cs_x Te$ bonding environment. The carbon present on the sample has been associated with CO components as they align with binding energies in the O 1s and C 1s spectra. The remainder of the oxygen on the photocathode surface is associated with Cs_2O.
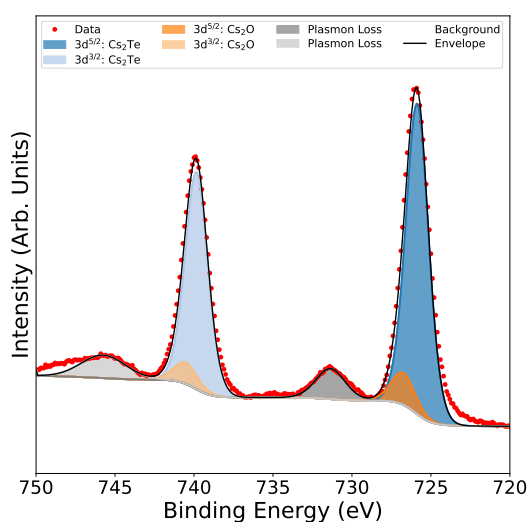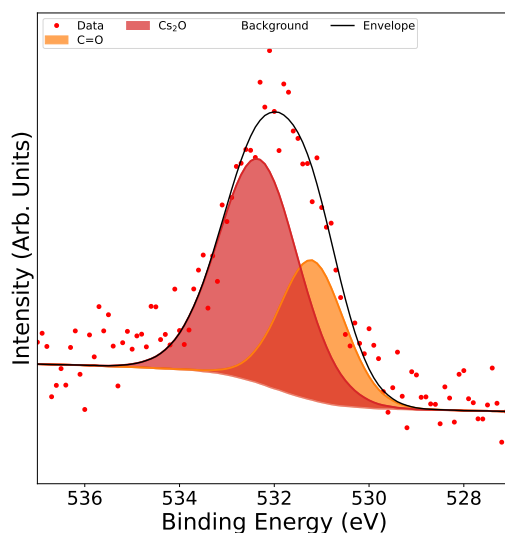

(a) Caesium 3d core region.
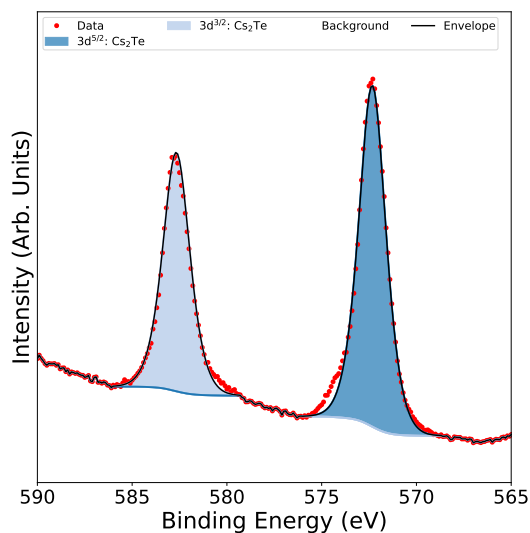
(b) Tellurium 3d core region.

(c) Carbon 1s core region.

(d) Oxygen 1s core region.

Figure 10: XPS Core peak profiles for the primary elements in the P6 photocathode showing their deconvolution and suggested bonding environment.

When considering the contaminants detected on the photocathode surface and the bonding environment data for Cs and Te, the atomic concentrations demonstrate an overall Cs:Te ratio of $49.16 : 35.34$, implying a compound ratio of $Cs_{1.4}Te$.

6.3   MTE Analysis

Fig. 12 shows the MTE values measured as a function of the illumination wavelength for the P6 Cs–Te photocathode at room temperature (red diamonds) and cryogenic temperatures (blue diamonds) of 181 K. The thermal floor at room temperature defined by $k_b T = 25$ meV is shown by the red chain–dotted line.

At room temperature the P6 photocathode shows a progressive decrease in MTE at UV wavelengths until 326 nm where the MTE plateaus across a small wavelength range before increasing between 346 nm and 356 nm. The MTE then gradually decreases once again until we see an increase for wavelengths beyond 396 nm, until we reach the emission threshold at 436 nm. This step–change at 400 nm may well be attributed to incomplete suppression of second–order light from the monochromator.

MTE Measurements were then taken under cryogenic conditions with the photocathode cooled to 181 K over the wavelength range 236 – 466 nm. The results followed a similar pattern to that seen for the room temperature data, with most data points exhibiting a reduced MTE over the UV wavelengths in comparison to the room temperature measurements. However we see that the MTE slightly exceeds that measured at room temperature for the longer wavelengths above 400 nm, with several other instances where the cryogenic MTE exceeds the room temperature MTE over the wavelength range $300 < \lambda < 400$ nm, though much of this variation can be attributed to the 10 % error bars n our measurements.

(a) Photoemission at 293 K.   (b) Photoemission at 181 K.
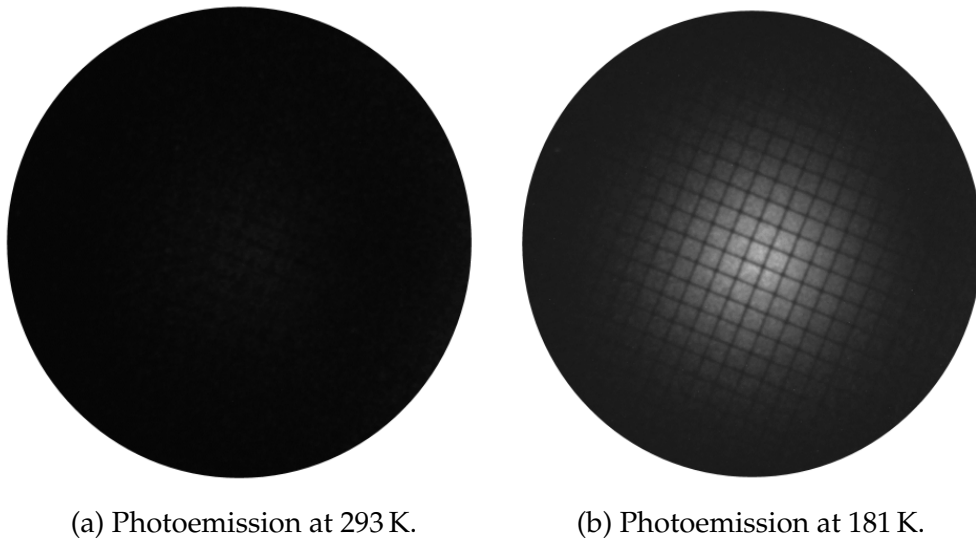
Figure 11: Comparison of the photoemission footprints recorded for the P6 photocathode under illumination at 436 nm.
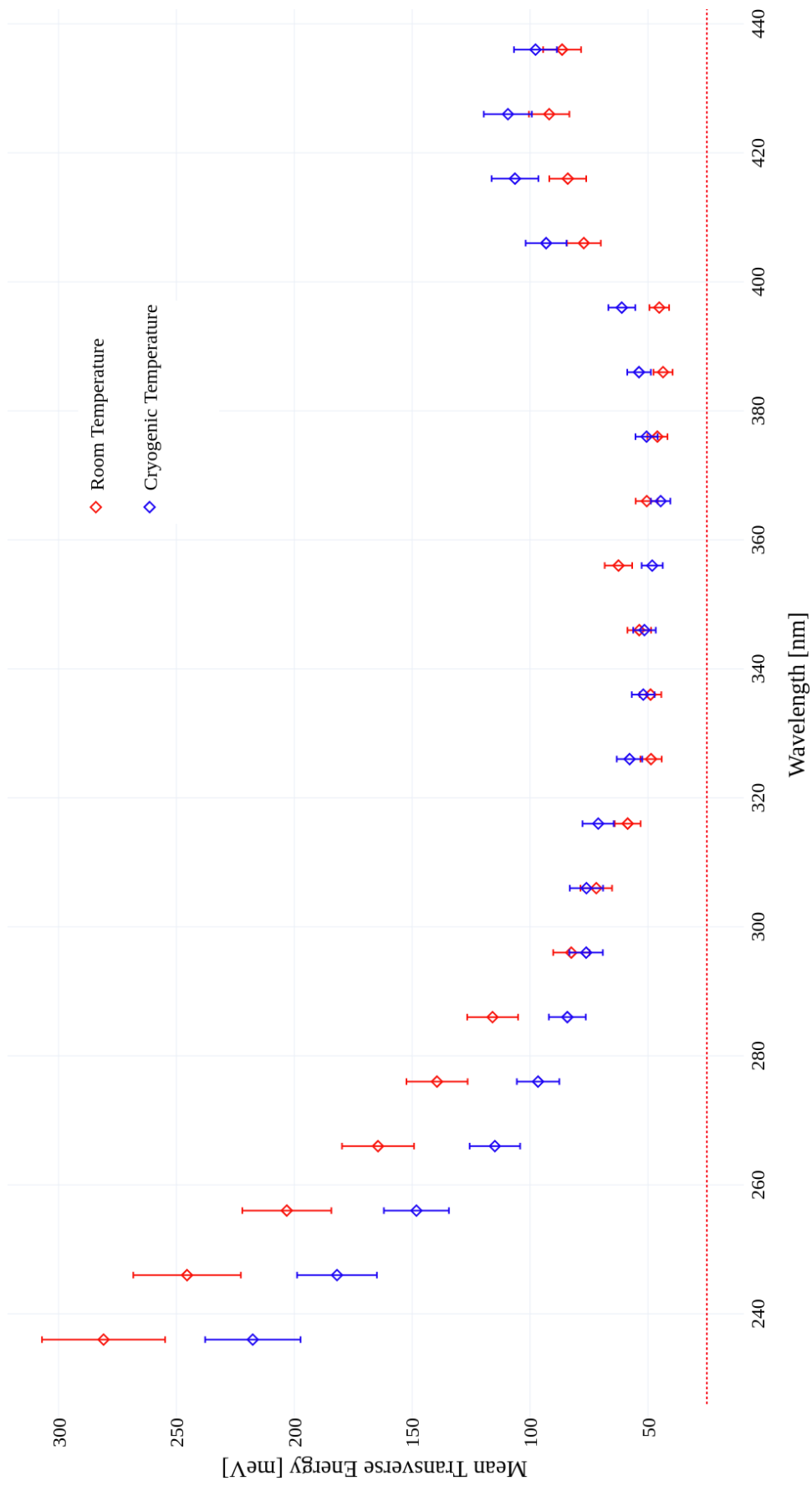
Figure 12: MTE measurements for the P6 CsTe photocathode under illumination at wavelengths between 236 nm and 436 nm for both room and cryogenic temperatures.

It was notable that when cooled, photoemission continued to longer wavelengths than seen at room temperature, as can be seen in Fig. 11 which compares the room temperature and cryogenic photoemission footprints at 436 nm. This increase in threshold emission wavelength may be attributed to the effect of cryo–pumping on the photoemissive layer whereby residual oxygen is fixed to the Cs–Te surface. This forms the highly–polar molecule CsO on the surface. Although the CsO contribution to the overall QE is low due to its low surface coverage, its presence will drive a significant increase in MTE as its low work function MTE increases the amount of excess energy in the photoemission process.

Fig. 13 shows the calculated relative QE for both the room and cryogenic data sets. Note that the data sets are not directly comparable in terms of the relative QE as some of the data points were taken with a different pixel cap setting in the data acquisition program.
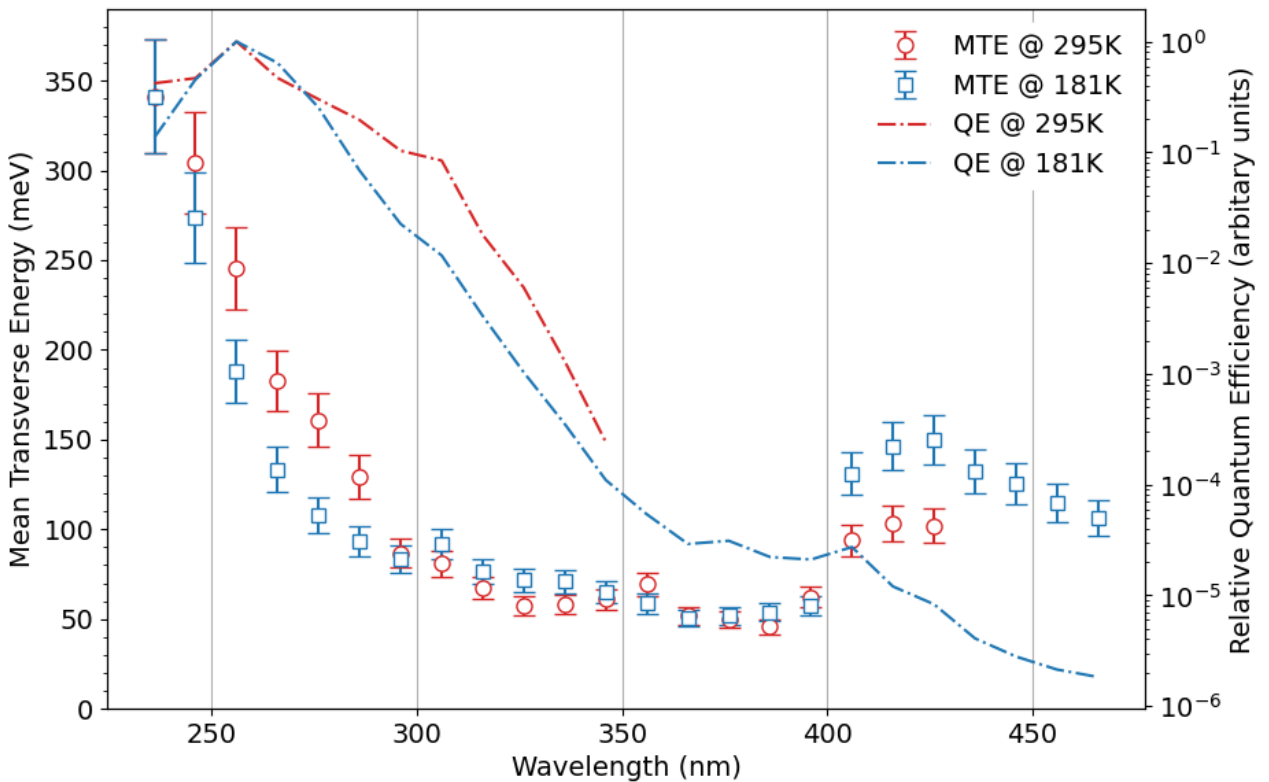
Figure 13: Comparison between extracted MTE values and estimated relative QE values based on known gain parameters and measured optical power at various illumination wavelengths ranging from 236 nm - 436 nm for the P6 CsTe photocathode at both room and cryogenic temperatures.

6.4 Quantum Efficiency Measurement

QE for the P6 photocathode was measured using the UV LED after all MTE and surface characterisation work had been completed. The data indicate that the absolute QE was 0.6 % at 265 nm.

7 P7 CsTe Cathode

7.1 XPS Surface Analysis

Table 6 shows the overall elemental composition for the P7 photocathode surface, and Table 7 shows the specific bonding environments of those elements present. Fig. 14 shows the core elemental regions of P7. Notable elemental peaks are labelled, showing Cs, Te and O present in the spectra.

Region	At Conc. [%]
Cs 3d	54.17
Te 3d	42.33
O 1s	3.49

Table 6: XPS overall elemental composition for the P7 cathode calculated from the core region components.

Region	Bonding Environment	Peak Position [eV]	FWHM	At Conc. [%]
Cs $3d^{5/2}$	Cs_xTe	725.04	1.67	48.50
$3d^{3/2}$		739.01	1.67	
$3d^{5/2}$	Cs_2O	725.95	1.70	5.68
$3d^{3/2}$		739.71	1.70	
Te $3d^{5/2}$	Cs_xTe	571.18	1.30	21.85
$3d^{3/2}$		581.55	1.40	
$3d^{5/2}$	Te	572.84	1.30	20.48
$3d^{3/2}$		583.19	1.40	
O 1s	Cs_2O	531.21	1.62	3.49

Table 7: XPS elemental composition for the P7 photocathode with bonding environments assigned according to the data–fitting shown in Fig. 14.
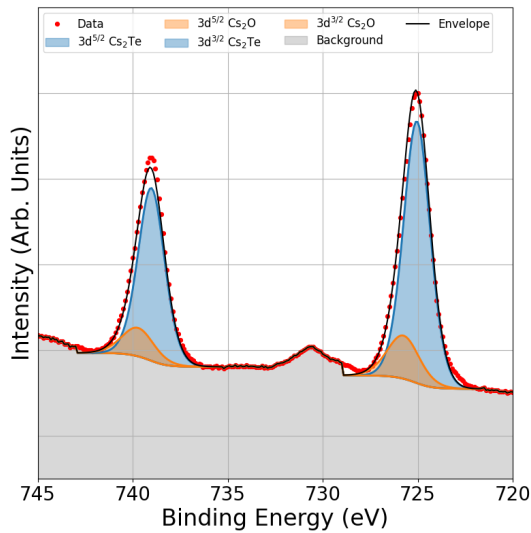
7.2 Bonding Environment Analysis

The XPS spectra acquired for the P7 cathode showed that the only contaminant present is oxygen with an atomic concentration of 3.49 %, all of which appears to be bound to Cs.

The Te 3d feature exhibits two distinct components, as can be seen in Fig. 14b. The peak positions strongly suggest Cs_xTe at 571.18 eV and elemental Te at 572.84 eV respectively. Oxygen present on the sample is not bound to Te due to the lack of a third peak at

around 576.1 eV or 577.0 eV. To fit the Te 3d feature and correctly account for both spin-orbit states, we first fitted the Te $3d^{5/2}$ feature, and then constrained the $3d^{3/2}$ fit with the same FWHM and two-thirds of the intensity for the $3d^{5/2}$ fit.

We deduce that the oxygen present on the sample is bonded only to the Cs. Information on the NIST XPS database [4] show that Cs forms a stable Cs_2O oxide. In our curve–fitting, we therefore introduced features at energies 725.95 eV and 739.71 eV with

(a) Caesium 3d core region.
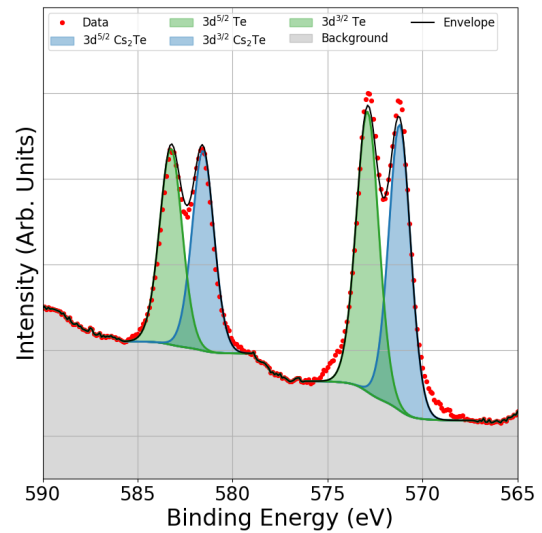
(b) Tellurium 3d core region.
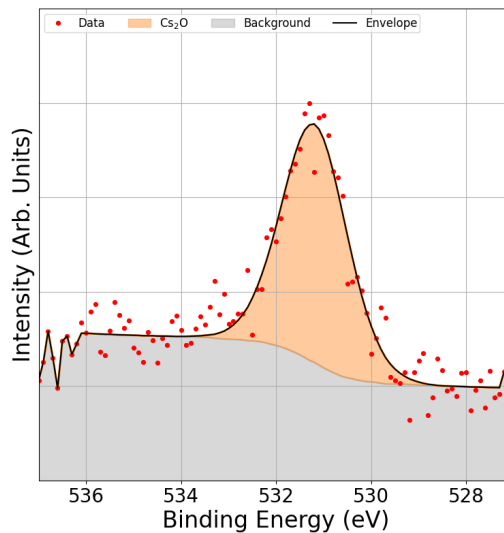
(c) Oxygen 1s core region.

Figure 14: XPS Core peak profiles for the primary elements in the P7 photocathode showing their deconvolution and suggested bonding environment.

the parameters stated in Table 7 for the $Cs\,3d^{5/2}$ and $Cs\,3d^{3/2}$ respectively. The atomic concentrations of the $Cs\,3d$ Cs_2O peaks show good agreement with the total concentration observed in the O 1s feature.

Excluding the elemental Te, the Cs_2O contamination detected on the photocathode surface and the bonding environment data for Cs and Te, we estimate the bonded Cs:Te ratio to be $48.50 : 21.85$, implying a compound ratio of $Cs_{2.2}Te$.

7.3 Surface Topography

Three positions on the P7 photocathode were characterised using STM to measure the surface roughness, as shown in Fig. 15. Position (a) is at the centre of the P7 cathode with
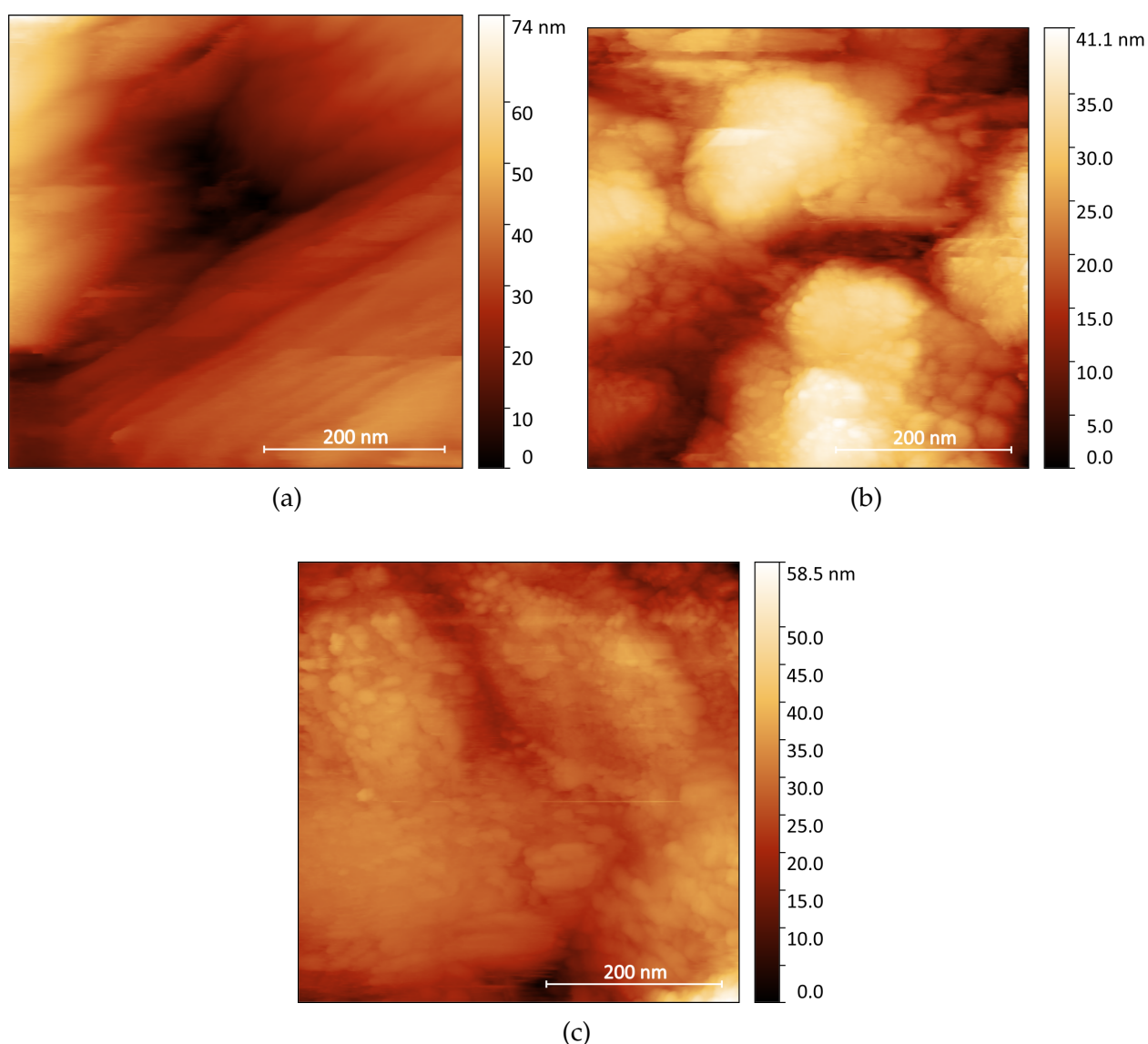

(a)

(b)

(c)

Figure 15: $500\,\text{nm} \times 500\,\text{nm}$ STM images at three positions on the P7 photocathode, with (a) measured at the geometric centre and (b) and (c) at increasing radial displacements.

positions (b) and (c) representing positions with increasing radial displacement from the centre. Table 8 summarises the RMS (R_q) and mean (R_a) roughness levels extracted from this data. The general levels of surface roughness are similar to those presented in Fig. 7 for the P5 photocathode, though the P7 has its highest level of roughness at the centre, with a progressive reduction in roughness with radial displacement.

Position	RMS Roughness, R_q [nm]	Mean Roughness, R_a [nm]
1	11.1	8.8
2	8.1	6.8
3	5.4	4.2

Table 8: Summary of surface roughness measurements for the P7 photocathode. Position '1' relates to the geometric centre of the photocathode, with '2' and '3' relating to positions with increasing radial displacement from the centre. All measurements were made by STM over a $500 \times 500 \, \mathrm{nm}^2$ area.

7.4   MTE Analysis

Fig. 16 summarises the MTE values measured as a function of the illumination wavelength for the P7 photocathode at room temperature (red diamonds) and cryogenic temperatures (blue diamonds) of 188 K.

At room temperature the P7 cathode exhibits a progressively decreasing MTE at UV wavelengths before reaching a minimum MTE value of $45.3 \pm 4.2 \, \mathrm{meV}$ at 376 nm. Photoemission continued until reaching the threshold wavelength at 396 nm. Measurements taken with the photocathode cooled to 188 K at wavelengths between 236 nm − 396 nm followed the same trend with MTEs generally lower than those measured at room temperature, as is expected given the narrowing of the Fermi distribution due to cooling of the photocathode. The minimum MTE of $40 \pm 3.7 \, \mathrm{meV}$ at 366 nm is substantially more than the thermal floor defined by $k_b T$ which equates to 25 meV at room temperature falling to around 15 meV at 181 K.

The presence of the highly–polar low workfunction species Cs_2O on the photoemissive surface as evidenced by the XPS data summarised in Table 7 is the most likely reason for this performance. Due to its low workfunction, the Cs_2O acts as a low QE component of electrons with a large MTE in the overall photoemitted electron distribution. Cs_2O will photoemit under illumination at very long wavelengths up to around 532 nm. This ever–present contribution is the reason why the thermal floor was not reached in either data set when the photocathode was illuminated at close to the threshold wavelength.
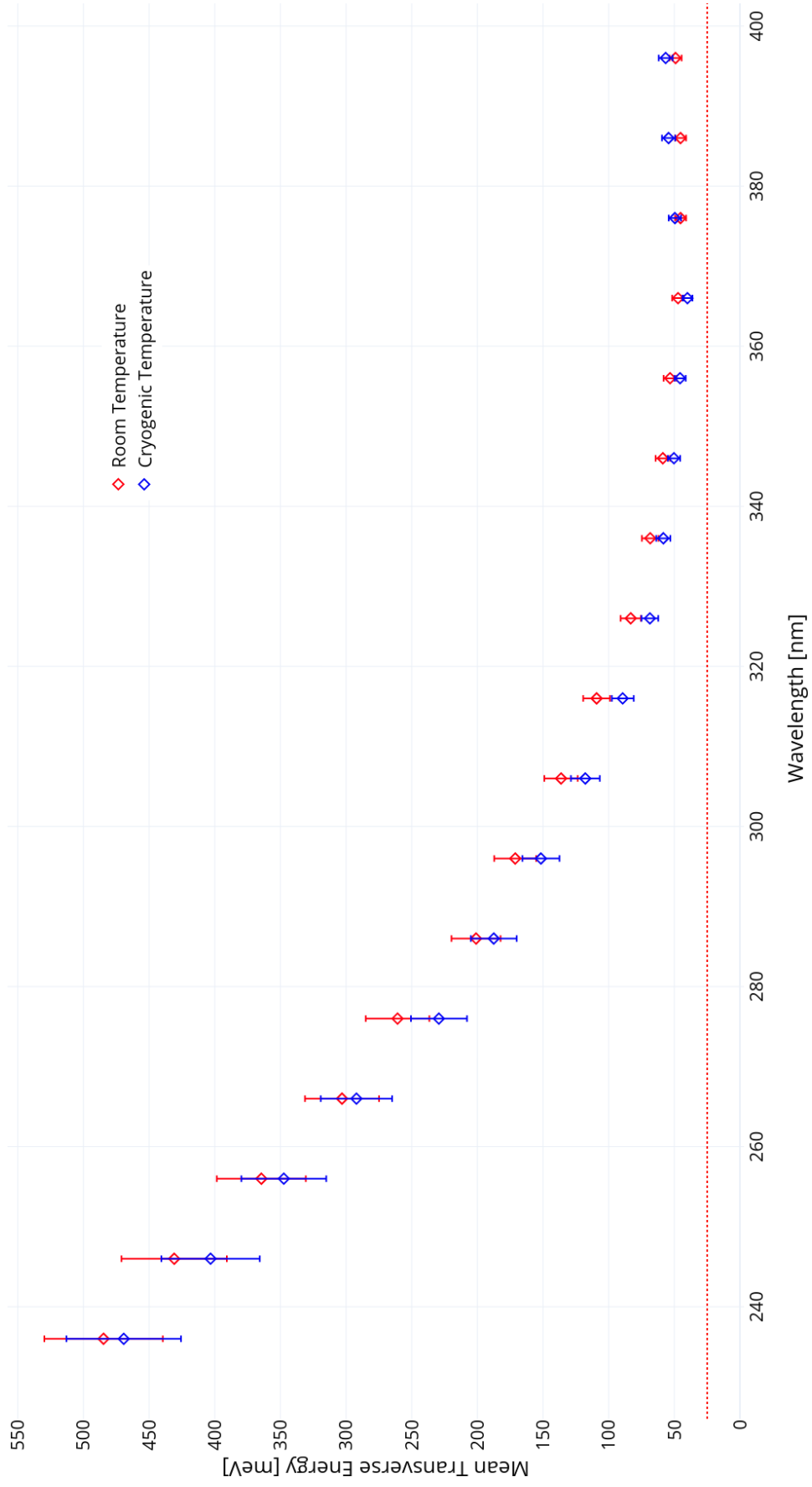
Figure 16: MTE measurements for the P7 CsTe cathode at various illumination wavelengths ranging from 236 nm – 396 nm at both room and cryogenic temperatures.
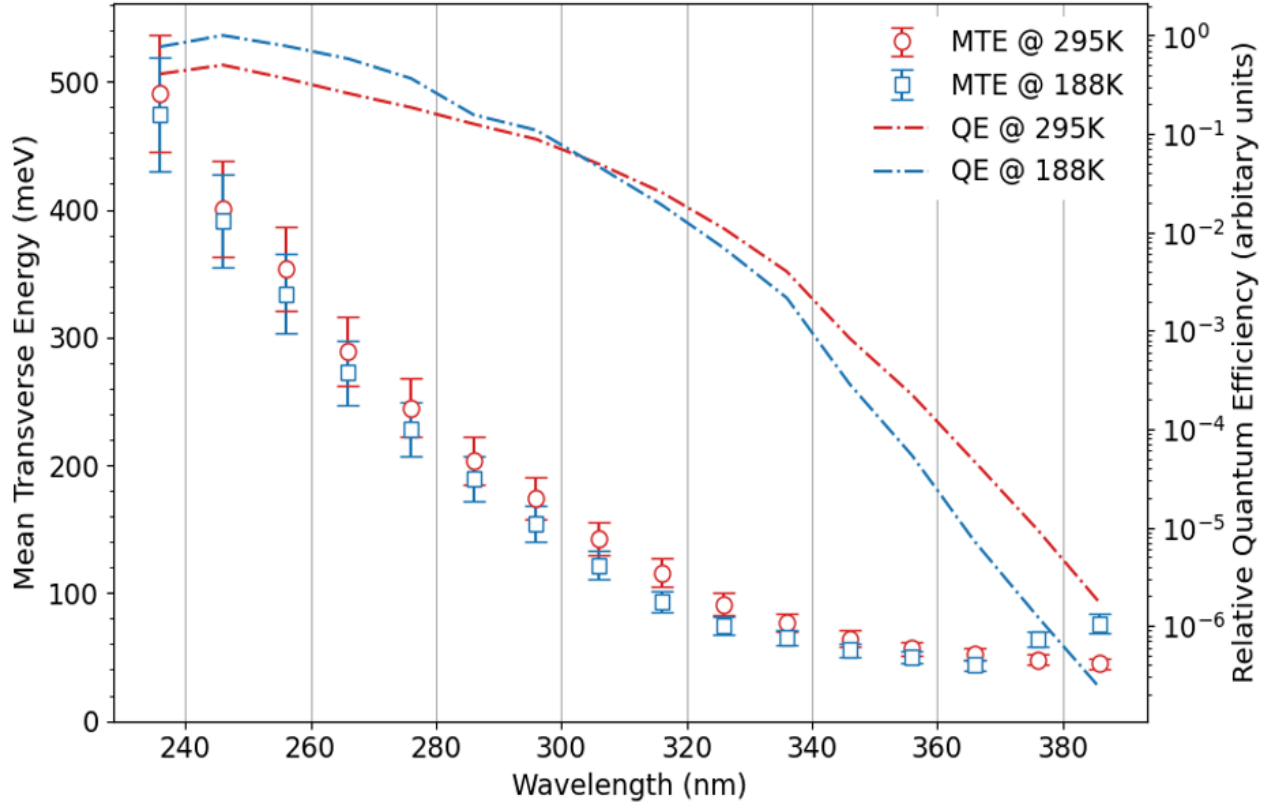
Figure 17: Comparison of the measured MTE and relative QE calculated using Equation (3) for the P7 photocathode under illumination at wavelengths between 236 nm and 396 nm at both room and cryogenic temperatures.

Fig. 17 shows the relative QE determined from the photoemission data for the P7 photocathode as described in section 4.1. In comparison to the other photocathodes, the P7 cathode exhibited the largest dynamic range in the relative QE calculated using Equation (3) covering 6 orders of magnitude over the range of illumination wavelengths investigated. The other photocathodes considered in this study exhibited a dynamic range covering only 4 orders of magnitude in the calculated QE.

7.5   Quantum Efficiency Measurement

QE for the P7 photocathode was measured using the UV laser after all MTE and surface characterisation work had been completed. The data indicate that the absolute QE was 0.2 % at 266 nm.

8   P8 CsTe Cathode

8.1   XPS Surface Analysis

Fig. 18 shows the core peak profiles for the P8 photocathode. The spectra only show elemental Cs and Te. Cathode P8 exhibited no oxygen or carbon in the survey and core regions scans, indicating that the sample was uncontaminated in comparison to those samples previously discussed. The relative abundance of Cs and Te (summarised in Table 9) are 51.07 % and 48.93 % respectively, implying a compound ratio of $Cs_{1.04}Te$. However, further analysis of the bonding environment explains the apparently high abundance of Te on the P8 photocathode surface.

Region	At Conc. [%]
Cs 3d	51.07
Te 3d	48.93

Table 9: XPS overall elemental composition for the P8 cathode based on the core regional components shown in Fig. 18.

Region	Bonding Environment	Peak Position [eV]	FWHM	At Conc. [%]
Cs $3d^{5/2}$	Cs_xTe	724.95	1.67	51.07
$3d^{3/2}$		738.92	1.67	
Te $3d^{5/2}$	Cs_xTe	571.18	1.30	19.34
$3d^{3/2}$		581.55	1.40	
$3d^{5/2}$	Te	572.84	1.30	29.57
$3d^{3/2}$		583.19	1.40	

Table 10: XPS elemental composition for the P8 photocathode with bonding environments assigned according to the data–fitting shown in Fig. 18.

8.2   Bonding Environment Analysis

Similar to the P7 photocathode, the Te 3d region for the P8 cathode shown in Fig. 18b exhibits two distinct bonding environments with peak positions displayed in Table 10. These can be attributed the elemental Te and Cs_xTe, where the Cs_xTe shifts from elemental Te by $-1.69\,eV$.

When fitting the Te 3d, careful consideration was given to correctly account for plasmon loss features which overlap with the Te core region. This was achieved by constraining the area of each $3d^{3/2}$ peak to two thirds of their respective $3d^{5/2}$ peak. The FWHM of the fitted peaks were also constrained, with the fitting parameters summarised in Table 10.

Due to the following factors:

- the reactivity of Cs, and particularly its affinity for oxygen;
- the relatively narrow FWHM used in peak fitting in comparison to those used in the spectra measured for cathodes P6 and P7;
- the relative abundance of Cs to Te;

the Cs was assumed to be fully–bonded to the Te on the sample and simply fitted with a single component for each spin orbit in the Cs 3d region, as shown in Fig. 18a. The lack of oxygen in the P8 spectra strongly suggests that there was no excess Cs present on this photocathode surface, and this assumption is reinforced when comparing its performance to the previous photocathodes.

When considering only the Cs and Te which are bonded together, the Cs:Te ratio shown in Table 10 is $51.07 : 19.34$, implying a compound ratio of $Cs_{2.6}Te$.

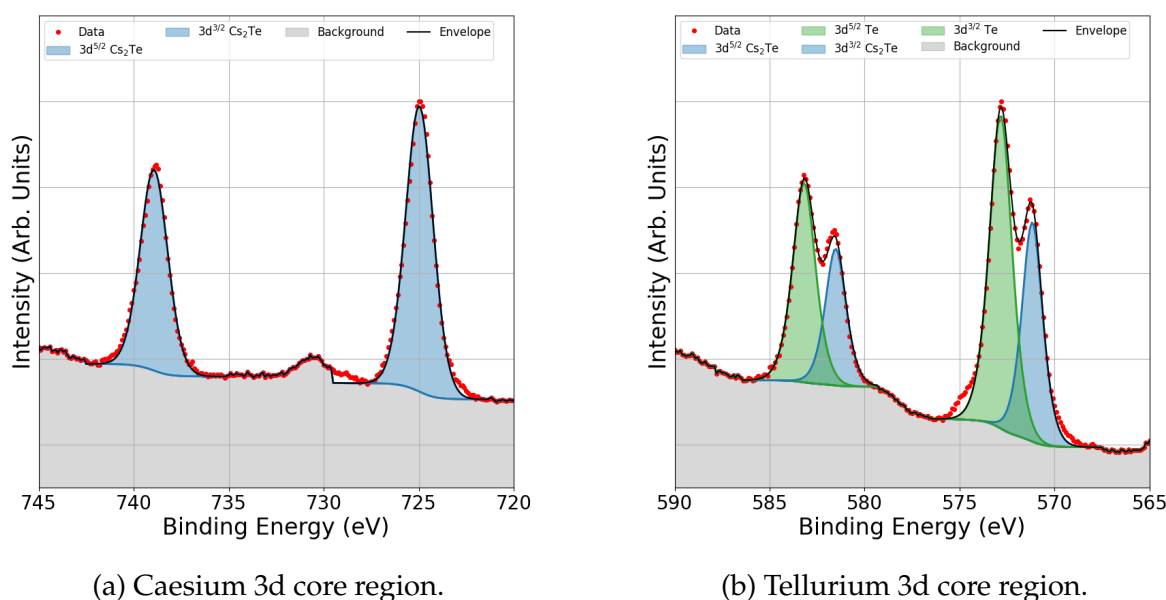(a) Caesium 3d core region. (b) Tellurium 3d core region.

Figure 18: XPS Core peak profiles for the primary elements in the P8 photocathode showing their deconvolution and suggested bonding environment.

8.3 Surface Topography

Surface roughness was measured using STM, with the expectation that three measurements would be carried out in the same way as that done for the P5 and P7 photocathodes. However, due to the failure of the STM tip, surface roughness was only measured at one position. Fig. 19 shows the STM image obtained at the centre of the P8 photocathode. The RMS surface roughness extracted from this data is 5.0 nm. This was the lowest level of surface roughness measured for the Cs–Te photocathodes prepared by CERN.
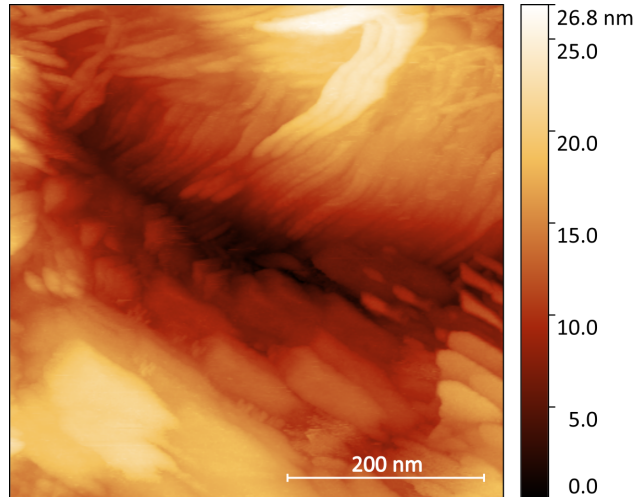
Figure 19: 500 nm × 500 nm STM image at the centre of the P8 photocathode.

8.4 MTE Analysis

Fig. 20 summarises the MTE values measured for the P8 Cs–Te photocathode as a function of the illumination wavelength at room temperature (red diamonds) and cryogenic temperatures (blue diamonds) of 191 K.

Under illumination at UV wavelengths at room temperature, the P8 cathode exhibits a progressively–decreasing MTE until 326 nm. At this point, there is a clear change in behaviour over a small wavelength range. The MTE at room temperature appears to plateau, though the scatter in the measured values is within the ±10 % error associated with TESS measurements. The MTE then continues to fall towards the thermal floor of 25 meV defined by $k_B T$. This transitory increase is more significant when the photocathode is cooled, though the behaviour remains the same with the MTE then falling progressively towards the thermal floor as the illumination wavelength is increased.

In both the room temperature and cooled datasets, the thermal is never achieved. The minimum MTE measured was 28.5 meV at room temperature under illumination at 426 nm, with 24.8 meV measured with the photocathode cooled to 181 K.

Photoemission data was taken at illumination wavelengths beyond 426 nm in order to determine where emission stops.

The relative QE shown in Fig. 21 follows a similar trend to that for the P7 photocathode as the illumination wavelength increases. The P8 photocathode has its emission threshold at a longer wavelength by some 40 nm than the P7 cathode.
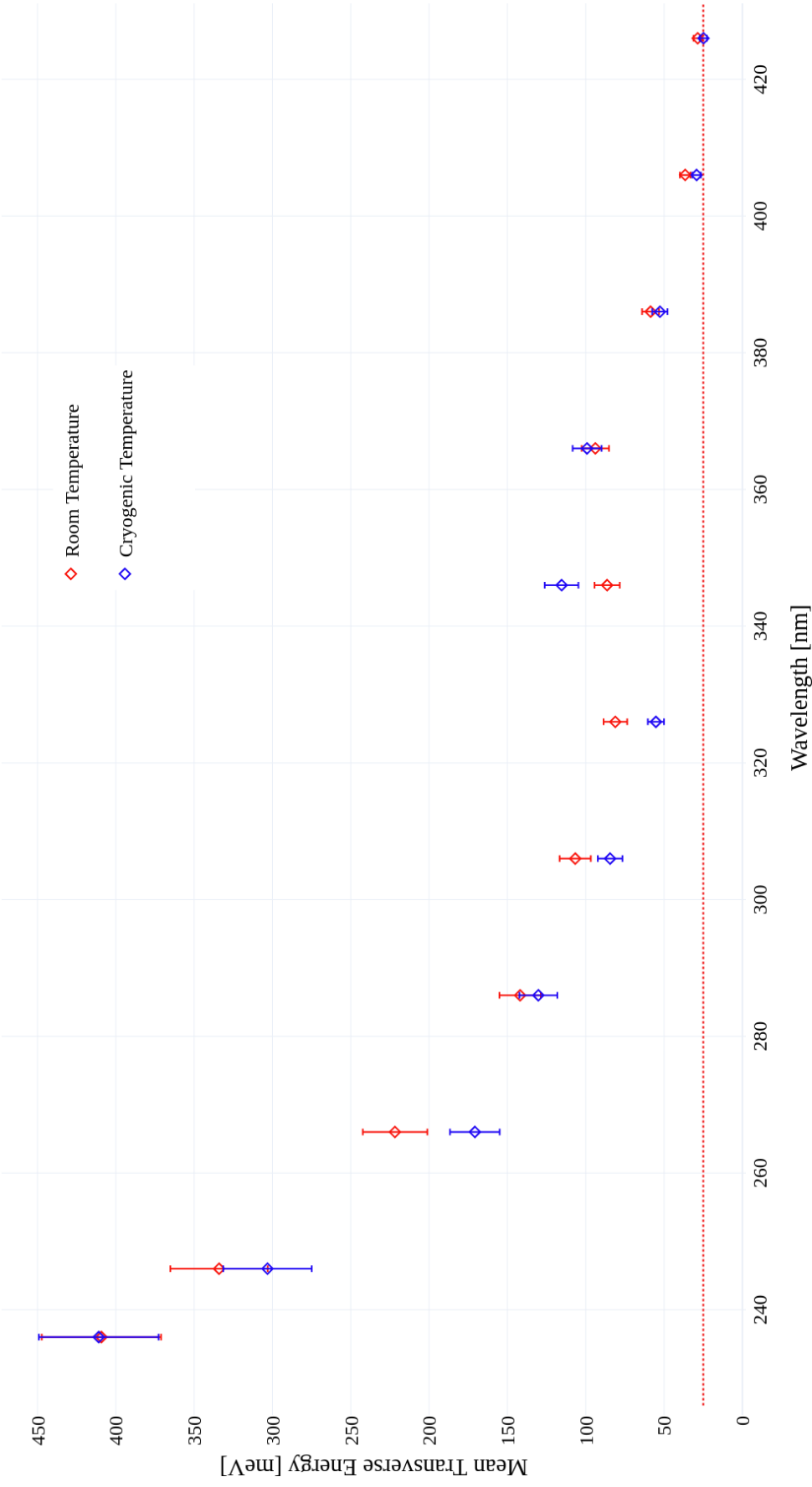
Figure 20: MTE measurements for the P8 CsTe photocathode at various illumination wavelengths ranging from 236 − 396 nm at both room and cryogenic temperatures.
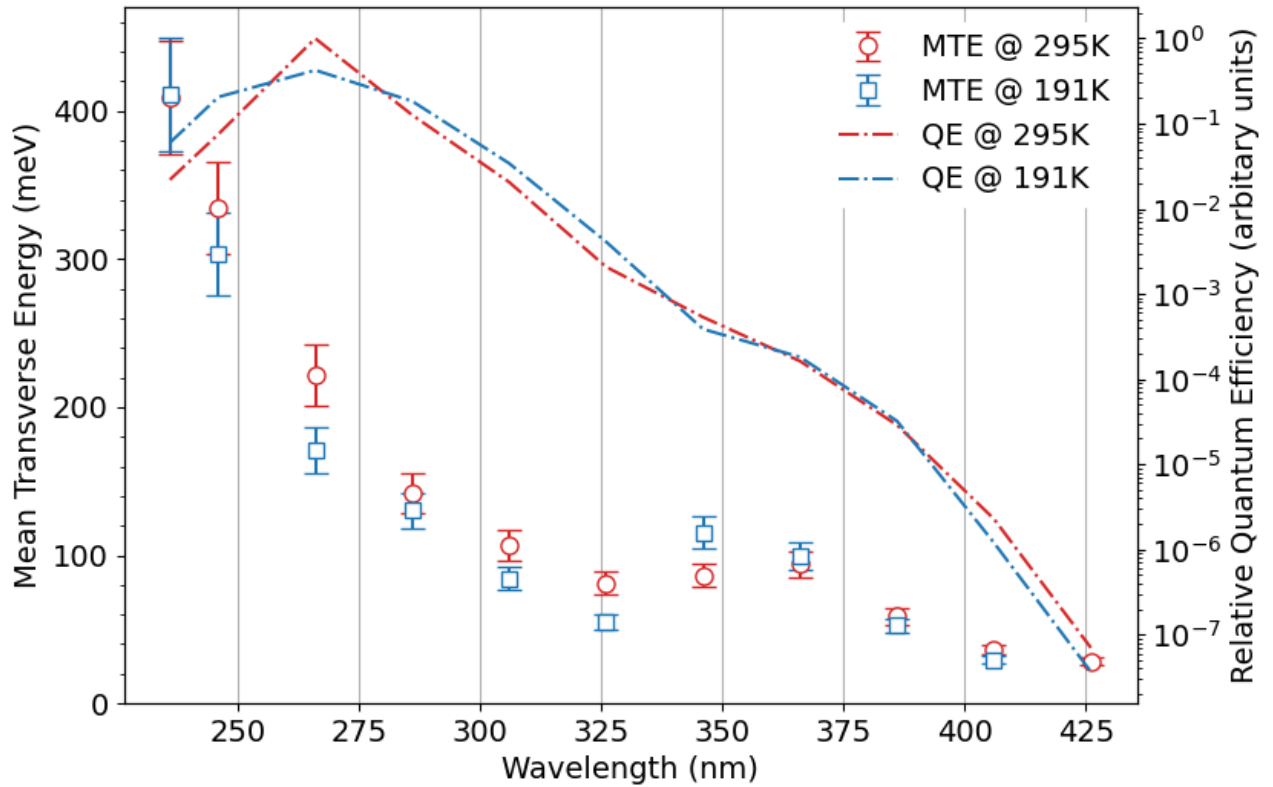
Figure 21: Comparison between extracted MTE values and estimated relative QE values based on known gain parameters and optical power for the P8 CsTe cathode at various illumination wavelengths ranging from $236 - 436\,\mathrm{nm}$ at both room and cryogenic temperatures.

8.5   Quantum Efficiency Measurement

QE was measured using the UV LED after all MTE and surface characterisation work had been completed. The data indicate that the absolute QE at 265 nm measured in May 2021 for the P8 photocathode was $QE_{265} = 2.9 \times 10^{-2}$ or approximately 2.9 %.

9 Summary of Results

This section summarises the main results obtained for the four photocathodes, P5 to P8. The gas exposure during transit approaching a level of 50 L combined with the delays in completing all of the planned work due to the sheer volume of the work and the delay associated with the dropping of the P5 photocathode in the TESS vacuum system have all contributed to substantial QE degradation. While the QE was not measured at CERN at the time of photocathode manufacture, CERN estimate that the QEs were in the 1 % – 10 % region, based on their previous experience. The only photocathode for which the QE was measured at DL suggested a figure in the region of 0.3 %, representing a substantial level of degradation since manufacture.

The XPS elemental analysis for the P5 photocathode which was exposed to atmosphere is presented in Table 11, and that for the P6, P7 and P8 photocathodes which were kept under vacuum for the duration of our work are presented in Table 12, which also shows the relevant bonding environments.

Region	Peak Position [eV]	RSF	At Conc. [%]
Cs 3d	724.70	38.73	14.06
Te 3d	573.15	29.91	4.65
C 1s	285.25	1.00	31.08
O 1s	530.90	2.85	50.21

Table 11: XPS compositional data for the P5 photocathode which was dropped inside the TESS following the completion of MTE measurements, and was subsequently exposed to atmosphere during its recovery.

Region	Bonding Environment	Cathode Atomic Concentration (%)		
		P6	P7	P8
Cs 3d	Cs_xTe	49.16	48.50	51.07
	Cs_2O	5.12	5.68	
Te 3d	Cs_xTe	35.34	21.85	19.34
	Te		20.48	29.57
O 1s	Cs_2O	2.07	3.49	
	C=O	4.13		
C 1s	C=O	4.18		

Table 12: Summary of XPS compositional data for the P6, P7 and P8 photocathodes with reference to the specific elemental bonding environments.

Table 13 summarises the quantum efficiency measurements made for the P6 – P8 photocathodes. These were carried out in the Multiprobe chamber following the completion of surface characterisation and MTE measurements.

Photocathode	P6	P7	P8
QE (λ)	0.6 % (265 nm)	0.2 % (266 nm)	2.9 % (265 nm)

Table 13: Summary of measured QEs for the P6 – P8 photocathodes.

Table 14 summarises the measured values for RMS surface roughness (R_q) and mean surface roughness (R_a) extracted from STM measurements. The cathodes were analysed in the order P5 $\rightarrow$ P7 $\rightarrow$ P8 $\rightarrow$ P6, as discussed in section 4.2, with the aspiration of taking three STM measurements for each photocathodes – one at the centre, and two at positions of increasing radial displacement. However, due to the failure of the STM tip and subsequent failure of the STM which prevent any further measurements, we were able to extract only a single STM surface roughness measurement for the P8 photocathode, and none at all for the P6.

There is a difference in trend between the P5 and P7 photocathodes, with the P5 having its lowest roughness at the geometric centre with roughness increasing with radial displacement. The opposite was true for the P7 photocathode which had its highest levels of roughness at the centre, with a progressive decrease in roughness as radial displacement increased. Based on the single measurement taken, P8 exhibited the lowest level of all in terms of surface roughness at the photocathode centre.

Photocathode	Position	RMS Roughness, R_q [nm]	Mean Roughness, R_a [nm]
P5	1	6.1	4.5
	2	12.3	10.5
	3	11.1	9.0
P6	N/A	N/A	N/A
P7	1	11.1	8.8
	2	8.1	6.8
	3	5.4	4.2
P8	1	5.0	4.1

Table 14: Summary of surface roughness measurements for the P5 – P8 photocathodes. Position '1' relates to the geometric centre of the photocathode, with '2' and '3' relating to positions with increasing radial displacement from the centre. All measurements were made by STM over a 500×500 nm^2 area.

Fig. 22 summarises the MTE data measured for the photocathodes at room temperature (298 K), and Fig. 23 summarises that for the cryogenic measurements made at temperatures ranging from 178 K to 191 K.
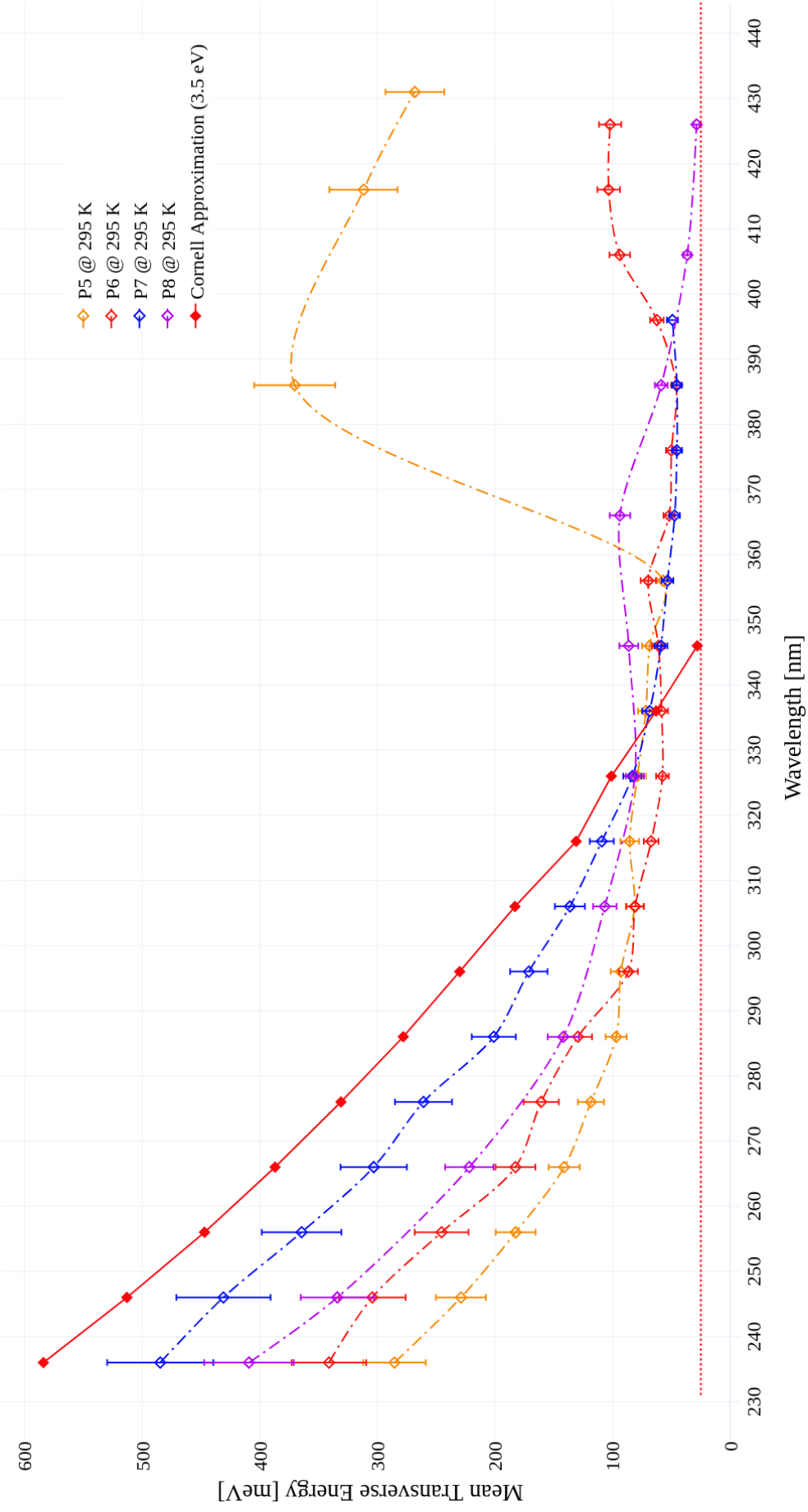
Figure 22: MTE measurements at room temperature for the P5, P6, P7 & P8 Cs–Te photocathodes under illumination at wavelengths between 236 nm – 436 nm.
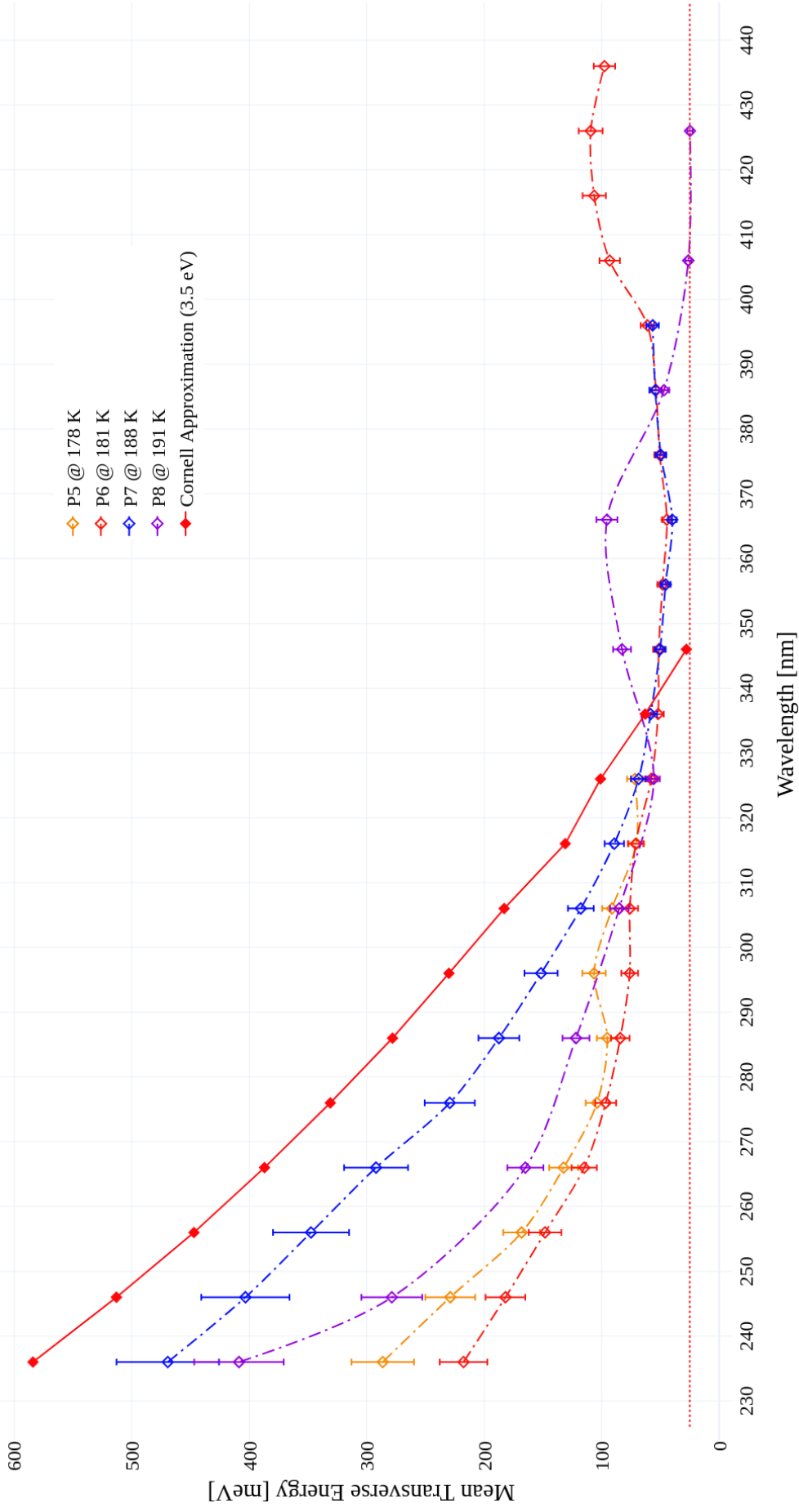
Figure 23: MTE measurements at cryogenic temperatures for the P5, P6, P7 & P8 Cs–Te photocathodes under illumination at wavelengths between 236 nm – 436 nm.

10 Discussion and Conclusions

The synthesis of Cs–Te cathodes and the difficulties therein is a topic which is well–covered by published photocathode literature. The challenges in the consistent manufacture of high–brightness photocathodes for particle accelerators which meet the required performance specifications is widely recognised [9, 14, 15].

At room temperature, caesium is known to form a family of stable compounds with tellurium (Cs_xTe_y) with a range of crystal structures and by extension, some variance in overall work function [16]. When the temperature is elevated, the Cs–Te system is known to exhibit an enhanced level of volatility with an even wider range of compounds formed, and a strong affinity to react with oxygen and water [17]. Caesium has a work function of 2.14 eV [18], and Cs_2O has an even lower work function with a value around 1.0 eV reported for a thin Cs_2O layer on silver, falling to around 0.6 eV for a thick layer [19].

On visual inspection, the Cs–Te photocathodes received at Daresbury exhibited a significant degree of variability, as can be seen in Fig. 4. The deposition data from CERN shown in Fig. 2 and summarised in Table 1 shows that there were substantial differences in the elemental deposition rates and total film thicknesses at the time of manufacture for each photocathode. This translates into visible differences under normal laboratory illumination conditions and ultimately performance differences when illuminated for photoemission. This variability continued into the analysis of the XPS and MTE datasets.

There is generally good consistency between the room temperature and cryogenic datasets for all of the photocathodes, with the MTE values measured when cooled being less than those at room temperature. However, the P8 photocathode is the only sample which reached the 25 meV thermal floor defined by k_BT, and even then only for the room temperature measurement. The cryogenic MTE measurement was slightly less than the room temperature measurement, but was still significantly more than the expected thermal floor at 191 K of 16 meV. What is clear from the MTE data is that all of the samples emit at illumination wavelengths longer than the conventionally–accepted photoemission threshold for a Cs_2Te photocathode, which varies over the range 320 to 350 nm depending on the deposition technique [9, 10].

The P5 photocathode emitted at the longest wavelengths, demonstrating measurable electron emission under illumination at wavelengths as long at 600 nm, albeit with the gain of the TESS system adjusted to a high level in order to detect this emission. However, due to the sample having been dropped inside the TESS and its subsequent exposure to atmosphere during its recovery, the XPS data we have on this photocathode cannot be meaningfully compared to that for the other photocathodes.

The oxygen detected on the P6 and P7 samples may be attributed to caesium's high level of reactivity and its affinity to form oxygen–containing compounds [17], but the lack of oxygen in the P8 XPS data is proof that this contamination did not occur during transportation in the vacuum suitcase. The oxygen must have been present at the time of photocathode manufacture, most likely in the form of water vapour at a low partial pressure in the deposition system at CERN.

The order of photocathode manufacture was P7, P5, P6 and finally P8. As can be seen from the XPS data summarised in table 12, the measured oxygen concentration fell as the manufacturing process progressed, suggesting that the deposition of caesium served

to fix any residual oxygen–containing species in the vacuum system and effectively remove this. Consequently the optimal deposition conditions existed at the time of the P8 manufacture.

Considering the measured presence of Cs_2O compounds with very low workfunctions [19] in the P6 and P7 photocathodes, and the likely presence of these on the P5 photocathode, coupled with the knowledge that the Cs layer on the P5 photocathode was the thickest of that applied in any of the deposition processes thereby leaving a substantial amount of low workfunction elemental caesium on the photoemissive surface, we believe that it is this combination of factors which has served to extend the spectral response of the P5, P6 and P7 photocathodes so dramatically. The smaller extension in spectral response for the P8 photocathode is most likely due to a simple excess of elemental caesium on the cathode surface. The low/very low workfunction of these chemical species serves to extend the spectral response and also amplify the energy spread, particularly at short illumination wavelengths where the excess energy is large for photoemission from these species.

Our XPS data also showed the presence of elemental tellurium on the P7 and P8 photocathodes. Tellurium has a work function of 4.95 eV [18], and this energy is not reached until the illumination wavelength is below 250 nm. Consequently, the presence of elemental tellurium does not have a detrimental effect on the photoemission performance. Furthermore, the detection of elemental tellurium is only possible in these samples due to the limited penetration depth of the XPS technique as the P6 photocathode had a thicker caesium layer than any of the other photocathodes, as summarised in Table 1.

A comparison of the RSF corrected XPS data for the 3d states in the Cs_xTe bonding environment shows that the Cs:Te ratio measured for the P6, P7 and P8 photocathodes are 1.4, 2.2 and 2.6 respectively. Given that caesium and tellurium are known to form a range of compounds [16], it is likely that these ratios give an insight into some of the other Cs_xTe_y compounds on the photoemissive surface (where $x \neq 2$ and/or $y > 1$), though our XPS system is not capable of resolving these subtle differences. There are no published values for the workfunctions of these higher–order compounds, so it is not possible to state with any degree of certainty the effect that this may have on the energy spread measured from a photocathode where the Cs:Te ratio differs substantially from the ideal value of 2.

It is notable that the summaries in Figs. 22 and 23 show each of the datasets initially behaving as expected, with each photocathode exhibiting a high level of MTE at short illumination wavelengths which falls progressively as the wavelength is increased. All of the datasets trend towards their respective thermal floor limit within the wavelength range specified above (300 to 350 nm [9]), but they do not actually reach this level and instead behave asymptotically or even increase further as the illumination wavelength increases. Given the obvious presence of photoemitting species other than Cs–Te on the surface, the mechanism behind this measured spectral response must be photoemission from compounds other than Cs_2Te, albeit at low levels of quantum efficiency.

While absolute QE measurements were only performed on the P8 cathode, the relative QE estimates based on Equation (3) for P5, P6 and P7 show that the QE of each cathode at longer wavelengths was extremely low. However, these quantities are non–vanishing and the photoemission contribution from the non Cs–Te elements remains detectable at the longer illumination wavelengths.

References

[1] T.C.Q. Noakes B.L. Militsyn, R. Valizadeh, K.J. Middleman, A.N. Hannah & L.B. Jones; EuCARD-2, CERN-ACC-2014-0039

[2] P. Ruffieux, P. Schwaller, O. Gröning, L. Schlapbach, P. Gröning, Q.C. Herd, D. Funnemann & J. Westermann; Rev. Sci. Inst. **71** (10), 3634 – 3639 (2000)

[3] N. Fairley, V. Fernandez, M. Richard–Plouet, C. Guillot–Deudon, J. Walton, E. Smith, D. Flahaut, M. Greiner, M. Biesinger, S. Tougaard, D. Morgan & J. Baltrusaitis; Appl. Surf. Sci. Adv. **5**, 100112 (2021)

[4] A.V. Naumkin, A. Kraut-Vass, S.W. Gaarenstroom & C.J. Powell; NIST X–ray Photoelectron Spectroscopy Database (2000); doi: 10.18434/T4T88K

[5] J.H. Scofield; J. Elec. Spect. **8** (2), 129 – 137 (1976)

[6] E. Chevallay; CERN CTF3 Note 104 (2012)

[7] E. Chevallay, M. Csatari, A. Dabrowski, S. Doebert, D. Egger, V. Fedosseev, O. Mete, M. Olvegaard, & M. Petrarca; J. Phys.: Conf. Series **347**, 012036 (2012)

[8] R. Xiang, A. Arnold, A. H. Buettig, D. Janssen, M. Justus, U. Lehnert, P. Michel, P. Murcek, A. Schamlott, Ch. Schneider, R. Schurig, F. Staufenbiel & J. Teichert; Phys. Rev. ST Accel. Beams **13**, 043501 (2010)

[9] M. Gaowei, J. Sinsheimer, D. Strom, J. Xie, J. Cen, J. Walsh, E. Muller & J. Smedley; Phys. Rev. ST Accel. Beams **22**, 073401 (2019)

[10] M. Gaowei; private communication; 2021

[11] B.L. Militsyn, I. Burrows, R.J. Cash, B.D. Fell, L.B. Jones, J.W. McKenzie, K.J. Middleman, H.E. Scheibler & A.S. Terekhov; Proc. IPAC'10, TUPE095, 2347 – 2349

[12] L.B. Jones, K.J. Middleman, B.L. Militsyn, T.C.Q. Noakes, D.V. Gorshkov, H.E. Scheibler & A.S. Terekhov; Proc. FEL2013, TUPS033, 290 – 293

[13] D. Nečas & P. Klapetec; Cent. Eur. J. Phys. **10** (1), 181 – 188 (2012)

[14] E. Prat, S. Bettoni, H.H. Braun, R. Ganter & T. Schietinger; Phys. Rev. ST Accel. Beams **18**, 043401 (2015)

[15] A. di Bona, F. Sabary, S. Valeri, P. Michelato, D. Sertore & G. Suberlucq; J. Appl. Phys. **80**, 3024 – 3030 (1996)

[16] G. Prins & E.H.P. Cordfunke; Journal of the Less-Common Metals **104** (1), L1 – L3 (1984)

[17] J. McFarlane & J.C. LeBlanc; Atomic Energy of Canada Ltd., Whiteshell Laboratories; Report № AECL-11333, COG-95-276-I (1996)

[18] H.B. Michaelson; J. Appl. Phys. **48**, 4729 (1977)

[19] J.J. Uebbing & L.W. James; J. Appl. Phys. **41**, 4505 (1970)